Article:

Holloway, MD, Sime, LC, Singarayer, JS et al. (2 more authors) (2016) Reconstructing paleosalinity from $\delta^{18}O$: Coupled model simulations of the Last Glacial Maximum, Last Interglacial and Late Holocene. Quaternary Science Reviews, 131 (B). pp. 350-364. ISSN 0277-3791

https://doi.org/10.1016/j.quascirev.2015.07.007

Reconstructing Paleosalinity from δ^{18}O: Coupled model simulations of the Last Glacial Maximum, Last Interglacial and Late Holocene

Max D Holloway[a,b], Louise C Sime[a], Joy S Singarayer[c], Julia C Tindall[d], Paul J Valdes[b],

[a] *Chemistry and Past Climate, British Antarctic Survey*
[b] *School of Geographical Science, University of Bristol*
[c] *Department of Meteorology, University of Reading*
[d] *School of Earth and Environment, University of Leeds*

Abstract

Reconstructions of salinity are used to diagnose changes in the hydrological cycle and ocean circulation. A widely used method of determining past salinity uses oxygen isotope (δ_{Ow}) residuals after the extraction of the global ice volume and temperature components. This method relies on a constant relationship between δ_{Ow} and salinity throughout time. Here we use the isotope-enabled fully coupled General Circulation Model (GCM) HadCM3 to test the application of spatially and time-independent relationships in the reconstruction of past ocean salinity. Simulations of the Late Holocene (LH), Last Glacial Maximum (LGM), and Last Interglacial (LIG) climates are performed and benchmarked against existing compilations of stable oxygen isotopes in carbonates (δ_{Oc}), which primarily reflect δ_{Ow} and temperature. We find that HadCM3 produces an accurate representation of the surface ocean δ_{Oc} distribution for the LH and LGM. Our simulations show considerable variability in spatial and temporal δ_{Ow}-salinity relationships. Spatial gradients are generally shallower but within ~50 % of the actual simulated LH to LGM and LH to LIG temporal gradients and temporal gradients calculated from multi-decadal variability are generally shallower than both spatial and actual simulated gradients. The largest sources of uncertainty in salinity reconstructions are found to be caused by changes in regional freshwater budgets, ocean circulation, and sea ice regimes. These can cause errors in salinity estimates exceeding 4 psu. Our results suggest that paleosalinity reconstructions in the South Atlantic, Indian and Tropical Pacific Oceans should be most robust, since these regions exhibit relatively constant δ_{Ow}-salinity relationships across spatial and temporal scales. Largest uncertainties will affect North Atlantic and high latitude paleosalinity reconstructions. Finally, the results show that it is difficult to generate reliable salinity estimates for regions of dynamic oceanography, such as the North Atlantic, without additional constraints.

Keywords: Paleosalinity, isotopes, oxygen-18, Last Glacial Maximum, Last Interglacial,

paleoceanography

1. Introduction

Discussion of past and future climate change is often difficult without reference to the oceanic global thermohaline circulation, a wind and density driven circulation of mass, heat and salt (Wunsch, 2002; Munk and Wunsch, 1998; Ferrari and Ferreira, 2011). The transition between cold glacial and warm interglacial periods has been linked to large changes in global ocean density structure (Adkins, 2013). At a given pressure, density is determined by seawater temperature and salinity via the equation of state. Patterns of ocean surface salinity also reflect patterns of surface water fluxes (evaporation and precipitation [E-P]) and have therefore been used to fingerprint changes in the global water cycle (e.g. Durack et al., 2012). Knowledge of past salinity is therefore important to characterise ocean circulation (Boyle, 2002; Adkins et al., 2002) as well as provide information on regional changes in hydrology (Stott et al., 2004; Durack et al., 2012). Although salinity can be measured in the modern ocean with very high accuracy, there are no direct measurements of past salinity before the historical era (Bingham, 2002). Thus, reconstructing past salinity changes in the ocean usually relies on proxies developed in marine sediment cores combined with a modern empirical calibration (Rohling and Bigg, 1998).

Oxygen stable isotopes (δ^{18}O reported in units of ‰ with respect to Vienna standard mean ocean water [VSMOW]) are a common tool in paleoceanography (e.g. Shackleton, 1974; Fairbanks, 1989; Broecker, 1989; Duplessy et al., 1993). Local changes in the δ^{18}O composition of seawater (δ_{Ow}) tend to be dependent on changes in freshwater and ocean circulation (Waelbroeck et al., 2014; Duplessy et al., 1991; Delaygue et al., 2001; Benway and Mix, 2004; LeGrande and Schmidt, 2006; Abe et al., 2009; Munksgaard et al., 2012). Hence, δ_{Ow} provides information about salinity changes and is indeed sometimes incorrectly called the 'salinity effect', given the tight coupling between salinity and δ_{Ow} (Delaygue et al., 2000, 2001; Rohling and Bigg, 1998; Rohling, 2000). On timescales relevant for ice sheet processes, a global ice volume effect (known as the glacial effect) also influences δ_{Ow} due to storage of the lighter isotope (^{16}O) in ice sheets. Global δ_{Ow} can therefore be used to reconstruct past global ice volume (Shackleton, 1967; Labeyrie et al., 1987; Fairbanks, 1989).

The δ_{Ow} of past seawater is not directly measurable. However, the δ^{18}O of $CaCO_3$ in shells (δ_{Oc}) can be measured from current and old foraminifera recovered from marine sediment cores (e.g. Shackleton, 1974; Fairbanks, 1989; Broecker, 1989). Values of δ_{Oc} are dependent on δ_{Ow}, seawater temperature, and species-specific offsets. Therefore, after species-specific corrections, measurements of δ_{Oc} can be used to reconstruct past seawater temperature if δ_{Ow} is known, or alternatively past δ_{Ow} can be reconstructed if temperature can be independently constrained (Waelbroeck et al., 2014). An on going challenge in paleoceanography has therefore been to separate δ_{Oc} into its individual temperature and δ_{Ow} components (Shackleton, 1967; Labeyrie et al., 1987; Chappell and Shackleton, 1986; Broecker, 1989; Cutler et al., 2003).

The δ_{Ow} residual method is the most commonly used approach for paleosalinity reconstruction (Rohling and Bigg, 1998; Rohling, 2000). This method assumes that, once a δ_{Ow} signal has been corrected for changes in global ice volume and the temperature signal has been independently constrained, the remaining δ_{Ow} anomaly relates linearly to changes in ocean salinity via a calibration between modern δ_{Ow} and salinity (e.g. Rostek et al., 1993; Weldeab, 2012; Hennissen et al., 2014; Broecker, 1989; Duplessy et al., 1991, 1993; Schmidt, 1999b; Duplessy et al., 1991). Early attempts to reconstruct paleosalinity assumed a globally uniform linear salinity versus δ_{Ow} gradient. A linear regression between modern salinity and δ_{Ow} measurements suggested a 0.5 ‰ increase in δ_{Ow} for a 1 psu increase in salinity (Craig and Gordon, 1965; Broecker, 1989; Duplessy et al., 1993). Although this gradient may be representative of a global average (Schmidt, 1999b), additional measurements of surface ocean properties have demonstrated that considerable geographical variability exists in this relationship (e.g. LeGrande and Schmidt, 2006; Conroy et al., 2014; Delaygue et al., 2001; McConnell et al., 2009; Bigg and Rohling, 2000; Schmidt, 1999a).

As these calibrations are generally derived under present day conditions (Schmidt, 1999a), they thus rely on the assumption that the controls on the proxy relationship have not changed through the past. This is known as the stationary assumption and is arguably the largest uncertainty in the use of modern proxy relationships (Stott et al., 2004; Rohling, 2000; LeGrande and Schmidt, 2011; Furtado et al., 2009). For example, measurements and model output suggest that the δ_{Ow}-salinity gradient can vary significantly over time due to local changes in sea ice cover, ocean circulation, and individual terms in the freshwater budget, such as local changes in the δ^{18}O of precipitation (e.g. Frew et al., 2000, 1995; Schmidt et al., 2007; LeGrande and Schmidt, 2011; Schmidt, 1999a; Leduc et al., 2013; Conroy et al., 2014; Rohling and Bigg, 1998; Benway and Mix, 2004). Further investigations are thus needed to test the validity of the stationary assumption.

Isotope enabled general circulation models (GCMs) allow isotopic variations to be interpreted beyond traditional single parameter reconstructions. The array of timescales accessible to models enables the stationary assumption to be rigorously tested. Isotope-enabled simulations have been used to reproduce the present-day climate (Tindall et al., 2009; Noone and Simmonds, 2002; Lee et al., 2007; Werner et al., 2011) as well as past climates, including warm interglacials (Schmidt et al., 2007; LeGrande and Schmidt, 2011; Masson-Delmotte et al., 2011; Sime et al., 2009, 2013; Tindall et al., 2010), and cold glacial climates, such as the Last Glacial Maximum (Lee et al., 2008; Roche et al., 2004; Caley et al., 2014). Indeed, the interpretation of surface temperature from ice core isotopic records has benefitted from isotope-enabled atmospheric GCMs (e.g. Noone and Simmonds, 2002; Jouzel et al., 2003; Sime et al., 2008, 2009, 2013; Masson-Delmotte et al., 2011). The inclusion of isotope tracers into oceanic GCMs has led to similar investigation of the relationship between seawater isotopes and salinity (e.g. Schmidt, 1999b; Delaygue et al., 2000). The δ_{Ow}-salinity relationship is a key test for fully coupled isotope modelling and has been used to explore the validity of the stationary assumption in response to changes in orbital forcing (Schmidt et al., 2007; LeGrande and Schmidt, 2011). However, holes still exist in the scope of timescales invested; paleosalinity modelling investigations have primarily focussed on warm interglacial periods (e.g. Schmidt et al., 2007; LeGrande and Schmidt, 2006, 2011; Tindall and Haywood, submitted; Russon et al., 2013). Therefore, the question of whether uncertainties are similar during periods of drastically different boundary conditions, such as glacial periods, is still very much open.

Here we explore the δ_{Oc}, δ_{Ow}, and salinity relationships using a set of water isotope (δ_{Ow}) enabled paleoclimate simulations. The simulations cover the key Last Glacial Maximum period, when major changes in the thermohaline circulation affected climate (Adkins, 2013; Adkins et al., 2002; Annan and Hargreaves, 2013; Ruddiman et al., 1984; Clark et al., 2009; MARGO Project Members, 2009), and the Last Interglacial period, the last climatic period with higher than present sea level (Kopp et al., 2009, 2013) and warmer than present temperatures (IPCC, 2013; Turney and Jones, 2010; Capron et al., 2014). The simulations enable us to characterise the magnitude of uncertainty induced by assumptions of geographical uniformity and stationarity. We outline the design of the model experiments and compare simulated ocean isotopes against observed δ_{Oc} records. We then examine the relationships between δ_{Ow} and salinity and test the application of spatially and time-independent relationships in the reconstruction of past ocean salinity; i.e. how large could errors in reconstructions of salinity over time be, if a gradient determined from the modern spatial δ_{Ow}-salinity distribution were to be used? The implications of our results, in terms of possible changes in the δ_{Ow}-salinity relationship through time, are then discussed.

2. Materials and Methods

2.1. Model Description

Experiments are set up using an isotope-enabled version of the Hadley Centre Coupled Model, version 3 (HadCM3) GCM. HadCM3 consists of a linked atmosphere, ocean and sea ice model and has been widely used to study past, present and future climates (e.g. Solomon et al., 2007; IPCC, 2013). The ocean component of HadCM3 is a rigid lid model based on Cox (1984). The ocean has a fixed volume and the model conserves water through salinity conservation. This study uses the isotope-enabled version of HadCM3 to investigate links between δ^{18}O and salinity. For a detailed description of the implementation of isotopes into HadCM3, the reader is referred to Tindall et al. (2009). Ice sheets and sea ice in the model are initialised with a δ^{18}O value of -40 and -2 ‰ respectively. The isotope component of HadCM3 ignores the small fractionation associated with sea ice processes and thus makes the approximation that sea ice melting/formation is non-fractionating (Tindall et al., 2009; Pfirman et al., 2004).

Model temperature and salinity have been evaluated in previous work for the modern climate (Gordon et al., 2000; Pardaens et al., 2003). Pardaens et al. (2003) concluded that the global hydrological cycle is well represented by the model, although its strength is overestimated compared to observations. Pardaens et al. (2003) observe a drift towards a more saline Atlantic Ocean throughout the simulation due to an overestimate of local evaporation. Gordon et al. (2000) evaluated the coupled model simulation of sea surface temperature (SST), sea ice and ocean heat transport, concluding a good representation, in broad agreement with observed estimates. A good balance between the ocean and atmosphere heat budgets results in no large SST drift and, consequently, no heat flux adjustments are required in HadCM3 (Gordon et al., 2000). Although there are drifts in salinity ($<$0.1 psu/100 years), the magnitude does not significantly effect the ocean circulation and thus do not impact on the coupled ocean-atmosphere simulation of climate (Gordon et al., 2000).

Isotopic output has been validated for both the atmosphere only (Sime et al., 2008) and the coupled ocean-atmosphere model (Tindall et al., 2009, 2010; Xinping et al., 2012). Isotopic output has been compared against the Global Network of Isotopes in Precipitation (GNIP) observational database (Tindall et al., 2009; Xinping et al., 2012), the Masson-Delmotte et al. (2008) 20th century Antarctic surface snow δ^{18}O dataset (Sime et al., 2008), and the Waelbroeck et al. (2005) dataset of Late Holocene planktic foraminifera δ_{Oc} (Tindall et al., 2010). Modelled isotope output captures the general spatial distribution of isotopes, including the latitude effect, amount effect, continental effect, and altitude effect, and is in good agreement with present-day observations (Tindall et al., 2009; Sime et al., 2008). Modelled ocean isotopes have been combined with model temperature output to compute δ_{Oc} and used to interpret pre-industrial coral (Russon et al., 2013) and ocean core records (Tindall et al., 2010). δ_{Ow} has been converted to δ_{Oc} using a variety of calibration equations and compared to ocean core top values, reproducing a zonal pattern that is in good agreement with data regardless of the chosen calibration equation (Tindall et al., 2010). The isotope component of HadCM3 has previously been used to investigate paleoclimates including the last interglacial (Sime et al., 2009, 2013), the Eocene (Tindall et al., 2010), the Pliocene (Tindall and Haywood, submitted), as well as periods of abrupt climate change (Tindall and Valdes, 2011).

2.2. Model Simulations

A Late-Holocene control simulation (hereafter LH) was run along with two sensitivity experiments; representing the period 21 thousand years BP (ka) and 125 ka. The period 21 ka represents the peak of the last glacial period, or the Last Glacial Maximum (hereafter LGM), a period of global cold and maximum ice sheet extent relative to the last glacial cycle (Adkins, 2013; Adkins et al., 2002; Annan and Hargreaves, 2013; Ruddiman et al., 1984; Clark et al., 2009; MARGO Project Members, 2009). In contrast, the period 125 ka corresponds to a minimum in global ice volume and characterises a period of global warmth during the last interglacial (hereafter LIG) (Dutton and Lambeck, 2012; Kukla et al., 2002; Shackleton et al., 2002; IPCC, 2013; Turney and Jones, 2010; Capron et al., 2014).

HadCM3 does not include interactive ice sheets, carbon cycle, or methane. Any changes in orbit, GHG, dust, ozone and ice sheet evolution must be prescribed. The prescribed boundary conditions for each model integration are outlined in Table 1. Our LH simulation was set up following pre-industrial control guidelines from the Paleoclimate Model Intercomparison Project (PMIP), with atmospheric gas composition set to values for 1850 years BP (CO_2 is 280 ppmv; CH_4 is 760 ppbv; and N_2O is 270 ppbv). Paleo changes in orbit and GHG concentrations are relatively well constrained. We adopt the same boundary forcing as applied by Singarayer and Valdes (2010) (see Table 1 for details). Sea level reconstructions suggest that sea levels were ~6 m higher than present during the last interglacial (Kopp et al., 2009, 2013). There is still large uncertainty as to the source and timing of this additional sea level contribution, with contributions likely from both Greenland and Antarctica (IPCC, 2013). Considering the magnitude of the sea level anomaly relative to the resolution of HadCM3, we follow the approach of Singarayer and Valdes (2010) and apply no ice sheet anomaly to our LIG simulation. For the LGM simulation, data suggest a roughly 120 m drop in sea level (Fairbanks, 1989). Again following Singarayer and Valdes (2010), we apply an LGM ice sheet configuration based on the ICE-5G model (Peltier, 2004) used in the PMIP Phase 2 (PMIP2; https://pmip2.lsce.ipsl.fr/pmip2/, Braconnot et al., 2007) and a number of simulations included in PMIP3 (http://pmip3.lsce.ipsl.fr/).

Isotopes are added to simulations with climates that have already been spun up with the respective boundary conditions. All of our simulations are initialised with an isotopic value of 0 ‰ for δ^{18}O in the atmosphere and ocean. Once isotopes had been initialised, the LH and LIG simulations were integrated for a total of 600 years and the LGM for 800 years. By the end of all three simulations, surface and deep ocean δ_{Ow} changes by <0.01 ‰/100 years. Table 1

2.3. Reconstructing salinity from δ_{Ow} residuals

To use δ^{18}O as a proxy for spatial or temporal paleo-climate reconstruction, the relationship between the proxy and the desired, but unobservable, variable is often defined by the gradient of a linear relationship (e.g. Sime et al., 2008). For example, in the case of salinity, where δ_{Ow} is the proxy and salinity (*S*) is the target variable, this would take the form $\delta_{Ow} = \alpha S + b$, where the gradient $\alpha = \Delta\delta_{Ow}/\Delta S$. By definition of the linear relationship, the intercept value, *b*, is an indicator of the freshwater end-member (δ_F), defined as the value of δ_{Ow} when *S*=0 (Delaygue et al., 2001; LeGrande and Schmidt, 2006; Munksgaard et al., 2012).

The slope of the relationship, α, can be applied to spatial or temporal δ_{Ow} and *S* observations to obtain either a spatial or temporal gradient; i.e. by selecting either a stationary point in time and observing the co-variability of δ_{Ow} and salinity across a defined spatial domain (the spatial gradient) or selecting a stationary point in space and observing the co-variability of δ_{Ow} and salinity at that location with time (the temporal gradient). The gradient of the linear regression between spatial or temporal δ_{Ow} and *S* is defined as α^{SPACE} and α^{TIME} respectively. Changes to the temporal gradient are therefore; $\Delta\alpha^{TIME} = \partial\alpha/\partial t$ at a single point, where *t* is time, and changes in the spatial gradient are; $\Delta\alpha^{SPACE} = \partial\alpha/\partial x$ at a single time, where *x* is a geographic location. The value of α^{SPACE} can be measured in modern ocean water and is the value that is traditionally applied when reconstructing past oceanographic changes, assuming that the spatial and temporal relationships are the same, i.e. $\alpha^{SPACE} = \alpha^{TIME}$.

In order to define a measure of α^{TIME} for each simulation, the methodology is applied to decadally averaged δ_{Ow} and salinity output and defined as $\alpha^{DECADAL}$. To assess the temporal variability of the δ_{Ow}-salinity relationship on long timescales, i.e. between simulations, α^{SLICE} is defined as; $\alpha^{SLICE}_{LGM-LH} = (\frac{\delta^{LGM}_{Ow}-\delta^{LH}_{Ow}}{S^{LGM}-S^{LH}})$ and similarly for α^{SLICE}_{LIG-LH}. Values of α^{SLICE} are calculated by averaging *S* and δ_{Ow} over the final 100 years of each simulation. α^{SLICE} represents the 'real' value for α (in model world) between the two climates and using this gradient will produce accurate estimates of past salinity. Therefore, because we only observe α^{SPACE} (and to a lesser extent $\alpha^{DECADAL}$) in the modern ocean, a perfect estimate of past salinity could be provided by the δ_{Ow} residual method if $\alpha^{SPACE} = \alpha^{DECADAL} = \alpha^{SLICE}$. Here, we test the extent to which this is true in model world. In the following sections we quantify the spatial and temporal bias in inferred salinity by evaluating the δ_{Ow}-salinity gradient during the LH, LGM and LIG, using the notation; α^{SPACE}_{LH}, α^{SPACE}_{LGM} and α^{SPACE}_{LIG} for spatial trends; $\alpha^{DECADAL}_{LH}$, $\alpha^{DECADAL}_{LGM}$ and $\alpha^{DECADAL}_{LIG}$ for intrinsic multi-decadal variability; and α^{SLICE}_{LGM-LH} and α^{SLICE}_{LIG-LH} to represent the simulated δ_{Ow}-salinity relationship on long glacial-interglacial timescales.

3. Results

3.1. Benchmarking modelled δ_{Ow}

The performance of the isotope-enabled HadCM3 is first evaluated against the patterns observed in marine sediment core δ_{Oc} records. We focus our benchmarking on the LH and LGM simulations as these time periods have most data coverage, can be accurately dated using ^{14}C, and have sufficient confidence levels on the data (Waelbroeck et al., 2005; MARGO Project Members, 2009; Waelbroeck et al., 2014; Caley et al., 2014).

To compare with marine sediment core foraminiferal calcite, modelled δ_{Ow} is converted to δ_{Oc} using the quadratic approximation of O'Neil et al. (1969), given in Shackleton (1974). Assuming that calcification temperature can be approximated by sea water temperature, modelled δ_{Ow} and ocean temperature (T) fields are used from the top model layer (0-5 m) to invert for δ_{Oc}:

$$\delta_{Oc} = \delta_{Ow} - 0.27 + 21.9 - \sqrt{310.6 + 10T} \tag{1}$$

The factor -0.27 is the conversion between scales, from SMOW to PDB, according to Hut (1987) (δ_{Ow} [VPDB] = δ_{Ow} [VSMOW] - 0.27). We recognise that the use of surface ocean properties will introduce bias when comparing to observed δ_{Oc} due to the variable depth habitat of different species of planktonic foraminifera. However, we find the choice of surface ocean depth has only minor affect on the following comparison. For comparative statistics, modelled δ_{Oc} is taken from the nearest model grid point to the equivalent ocean core location. This means that our comparison is weighted to the non-uniform geographic distribution of available measurements. Figure 1

We compare modelled surface ocean δ_{Oc} against planktonic foraminifer calcite δ_{Oc} (Figure 1). The LH simulation is compared against the Late Holocene data synthesis of Waelbroeck et al. (2005). This synthesis forms a Late Holocene time slice as part of the Multiproxy Approach for the Reconstruction of the Glacial Ocean surface (MARGO) project (MARGO Project Members, 2009) and is chronologically defined as the last 4 ka. For the LGM, modelled δ_{Oc} anomalies are compared against the compilation of Caley et al. (2014). Caley et al. (2014) report anomalies as the difference between mean δ_{Oc} between 19-23 ka for the LGM and the last 3 ka for the LH.

Figure 1 shows a strong latitudinal trend in both modelled and observed δ_{Oc}. Values are enriched in high latitude oceans and become progressively depleted towards the equator. This trend reflects the temperature dependent fractionation of calcification, approximately equalling a 0.2 ‰ depletion per °C increase in temperature (O'Neil et al., 1969). Consequently, the inverse of δ_{Oc} closely approximates the merdional temperature gradient of surface waters. A strong temperature dependence is also evident in LGM δ_{Oc} anomalies, which, after subtracting the glacial effect of 1 ‰ (see section 3.1.3.; Schrag et al., 1996; Adkins et al., 2002; Duplessy et al., 2002; Schrag et al., 2002), are positive over much of the global surface ocean, reflecting cooler glacial sea surface temperatures. In contrast, LGM δ_{Oc} anomalies are negative in the high latitude Arctic. Meteoric waters, which feed surface and subsurface runoff, are more depleted than surface ocean δ_{Ow}. During the LGM, high-latitude meteoric waters are significantly more depleted than during the LH and, consequently, act to deplete δ_{Ow} in the surface ocean. This effect is amplified close to Arctic coastlines due the direct influence of glacial runoff. Therefore, strong negative δ_{Oc} anomalies around the peripheries of the Eurasian ice sheet reflect highly depleted surface water δ_{Ow}.

Overall for the Late Holocene, planktonic foraminifera data compare well with modelled surface δ_{Oc}, producing a Root Mean Squared Error (RMSE) of 0.82 ‰. A small negative bias is evident from modelled δ_{Oc}, with a Mean Bias Error (MBE) of -0.27 ‰. This bias is significant in the mid-latitudes of the North Atlantic, where the model is more depleted than observations (Figure 1). However, modelled δ_{Oc} shows a small positive bias in the Greenland, Iceland, Norwegian (GIN) seas and the Arctic Ocean, where modelled δ_{Oc} values are more enriched than planktonic foraminifera δ_{Oc}. The Waelbroeck et al. (2005) dataset was chosen as it provides the largest spatial coverage. More recent Late Holocene syntheses have been modified to increase the data confidence but this also reduces the quantity of data points (e.g. Waelbroeck et al., 2014; Caley et al., 2014). Comparing the model to more recent compilations improves the RMSE to 0.66 and 0.77 ‰ for the Waelbroeck et al. (2014) and Caley et al. (2014) Late Holocene datasets respectively, but provides less information about spatial patterns. Waelbroeck et al. (2005) state the δ_{Oc} composition of fossil foraminifera in the MARGO dataset to be 0.2-0.8 ‰ more enriched than that of living foraminifera.

This bias is related to the stratification of upper ocean waters and decreases with latitude (Waelbroeck et al., 2005). This offset could in part explain the small negative bias observed in modelled LH δ_{Oc} (-0.24 ‰).

For the LGM, the model again compares well with observed δ_{Oc} anomalies and produces a smaller RMSE of 0.61 ‰. Subtraction of the glacial effect removes most of the model bias for the glacial climate (MBE = -0.07 ‰). An ongoing paleoclimate debate surrounds the disagreement between models and data regarding the glacial North Atlantic zonal δ_{Oc} gradient (Braconnot et al., 2007; MARGO Project Members, 2009). The model simulates strongly enriched LGM δ_{Oc} in the western Atlantic, decreasing towards the east. Once the data has been corrected for the global ice volume effect, observed anomalies are closer to zero in the west and increase towards the east. Similarly large positive model anomalies are observed in the North Pacific, associated with changes in the Kuroshio Current. However, a lack of data coverage in the central North Pacific precludes any assessment of this features accuracy. In the North Atlantic, the large positive anomalies during the LGM are associated with a southward shift of the Gulf Stream and intensification of the Subpolar Gyre. This region is no longer characterised by warm waters advected from the Florida Coast and is instead replaced by a strong Labrador Current advecting cold waters from the north. The positive δ_{Oc} anomalies therefore reflect surface ocean cooling. The model disagreement with marine core δ_{Oc} may thus be due to a poor simulation of the glacial Gulf Stream. Previous work has noted the stronger and more zonal Gulf Stream simulated by HadCM3 during the LGM (Hewitt et al., 2003), which is in disagreement with some reconstructions (e.g. Lynch-Stieglitz et al., 1999).

For the LH, a significant model-data disagreement exists in the GIN seas and the high latitude Arctic. Foraminiferal blooms in these regions will be strongly seasonal due to light limitation. Schmidt and Mulitza (2002) found the standard error of modelled coretop δ_{Oc} decreased from 1.2 ‰, when assuming annual average mixed layer equilibrium calcite, to 0.53 ‰, when combined with their ecological model, including parameters for species temperature ranges, optimum temperatures, depth habitat, and amount of secondary calcification. Our model calculated δ_{Oc} does not account for these factors. However, observed δ_{Oc} values can be compared against simulated summer δ_{Oc} (JJA for the northern hemisphere and DJF for the southern hemisphere) to test the effect of seasonality, assuming that δ_{Oc} is primarily a summer signal. Using simulated summer δ_{Oc} has negligible effect on the LGM comparison (RMSE and MBE of 0.58 and -0.09 ‰ respectively) and slightly worsens the LH comparison (RMSE and MBE of 0.96 and -0.54 ‰ respectively). Other areas of model-data disagreement are concentrated in regions of dynamic oceanography and sharp oceanographic fronts. Model resolution limits the accurate simulation of δ_{Oc} in regions such as the North

Atlantic and regions characterising water mass boundaries due to the presence of sharp property gradients. This considered, the model appears to simulate a polar front extent that largely agrees with the data in the North Atlantic and the Atlantic sector of the Southern Ocean, indicated by sharp horizontal gradients in δ_{Oc}. Despite local discrepancies, the model-data comparison suggests a good overall representation of Late-Holocene and LGM δ_{Oc} simulated by the isotope-enabled HadCM3 model.

Although a compilation of δ_{Oc} is not available for the LIG, the model suggests a similar surface ocean δ_{Oc} distribution between the LIG and LH (Figure 1 bottom panels). LIG δ_{Oc} is slightly more enriched in the tropics in response to the higher obliquity component during the LIG, and slightly more depleted around the coast of Greenland, reflecting changes in sea ice regime in response to the higher summer insolation.

3.1.1. The glacial effect

The bias between the LGM modelled and observed δ_{Oc} for the surface ocean can in part be explained by the uncertainty in quantifying the glacial effect ($\Delta\delta_g$). The precise value of the glacial effect is not well constrained. Early work suggested an enrichment of $\Delta\delta_g = 0.012z_{sl} \pm 0.001‰$, where z_{sl} is the sea level drop in meters (Labeyrie et al., 1987; Shackleton, 1987; Fairbanks, 1989; Rohling, 2000). The uncertainty suggests a range for $\Delta\delta_g$ of 1.32 to 1.56 ‰ for a 120 m drop in sea level. However, Schrag et al. (1996) argued that $\Delta\delta_g = 0.008z_{sl}$ is more appropriate. More recently, a number of approaches have converged towards the latter estimate, establishing a mean ocean δ_{Ow} enrichment for the LGM of 1.0 ± 0.1 ‰ (Schrag et al., 1996; Adkins et al., 2002; Duplessy et al., 2002; Schrag et al., 2002). The full uncertainty in $\Delta\delta_g$ is difficult to constrain, particularly because it is influenced by the size and isotopic composition of glacial reservoirs (Sima et al., 2006).

Because the model simulations were initialised with a δ_{Ow} value of 0 ‰, the discrepancy between modelled and observed δ_{Oc} can be used to suggest a model 'best fit' value for the glacial effect (e.g. Thresher, 2004), if we assume an otherwise perfect simulation of LGM δ_{Oc} and that the uncertainty in $\Delta\delta_g$ is the only cause of model-data disagreement. The mean data-model error for the LGM provides a value for the glacial effect; $\Delta\delta_g = (\overline{\delta_d} - \overline{\delta_m})$ where $\overline{\delta_d}$ and $\overline{\delta_m}$ are the mean LGM data and model isotopic composition at the core site locations respectively. Dividing $\Delta\delta_g$ by the inferred sea level fall in meters then gives a value for the glacial enrichment per meter of sea level change; i.e. $\eta = \frac{\Delta\delta_g}{z_{sl}}$, where η is the value for the isotopic enrichment per meter of sea level lowering. Solving this relation for the planktonic LGM data produces a value for $\Delta\delta_g$ of 1.08 ‰, and a value of η of 0.009 ‰/m for both annual average and summer-only modelled δ_{Oc}. This value of $\Delta\delta_g$ sits between the range of previously suggested LGM glacial enrichments, of 0.9 to 1.56 ‰.

3.2. Paleosalinity - δ_{Ow} residual method

In this section, the methodology set out in section 2.3. is applied to model salinity and δ_{Ow} output to evaluate both spatial (α^{SPACE}) and temporal ($\alpha^{DECADAL}$ and α^{SLICE}) relationships. We first assess the regional patterns of α^{SPACE} for the LH followed by the variability in the δ_{Ow}-salinity relationship during the LGM and LIG.

3.2.1. Spatial variability in the δ_{Ow}-salinity relationship

Modelled LH α^{SPACE} is compared to present-day observations from the Global Seawater Oxygen-18 Database (Schmidt, 1999b; Bigg and Rohling, 2000, http://data.giss.nasa.gov/o18data/) (Figure 2). Enclosed seas are masked for the comparison. Modelled regional δ_{Ow}-salinity relationships for each simulation are presented in Table 2, including the gradient (α^{SPACE}), the intercept (δ_F) and associated r^2 values from the spatial least squares linear regression. Figure 2

Variability in salinity and δ_{Ow} is larger in the observations than the model (Figure 2). This will in part be due to model resolution smoothing out variability and, even though enclosed seas have been masked, most of the observations lie in coastal regions affected by fresh and depleted continental and river runoff. Observed gradients decrease in most regions when data within one grid cell of the coastlines are masked (not shown). Including all model grid points within each region, and not only where observations are available, HadCM3 simulates an open ocean (excluding marginal seas, the Arctic Ocean poleward of 60°N and the Southern Ocean poleward of 60°S) α^{SPACE} of 0.18 ‰/psu for the LH (data 0.23 ‰/psu). If all observed and modelled ocean data are included in the analysis, δ_F becomes more depleted (from -8 to -13 and -6 to -7 ‰ for the observations and model respectively) and the gradients steepen (from 0.23 to 0.38 and 0.18 to 0.21 ‰/psu respectively). The simulated values lie within previous estimates of the δ_{Ow}-salinity gradient and intercept for the major ocean basins (LeGrande and Schmidt, 2006). In the Southern Ocean, the freshwater endmember is less depleted than other regions as it trends towards the value of sea ice melt water, prescribed in the model as -2 ‰ (Table 2; Southern Ocean LH δ_F = -2.45 ‰). This affect, plus the over-active hydrological cycle in HadCM3 (Pardaens et al., 2003), helps explain the shallow gradients simulated in mid and high-latitudes.

Spatial patterns in the δ_{Ow}-salinity relationship remain similar between the LH and LIG simulations, but change significantly for the LGM. α^{SPACE} remains similar in the glacial tropics but shows large and

	OBS			LH			LGM			LIG		
Region	α^{SPACE}	δ_F	r^2	α^{SPACE}	δ_F	r^2	α^{SPACE}	δ_F	r^2	α^{SPACE}	δ_F	r^2
All Ocean	0.39	-13.40	0.80	0.21	-7.14	0.69	0.19	-6.35	0.34	0.22	-7.54	0.71
Open Ocean	0.23	-8.04	0.60	0.18	-5.97	0.89	0.10	-3.35	0.54	0.17	-5.74	0.85
Tropics (30N-30S)	0.16	-5.11	0.72	0.18	-5.99	0.89	0.16	-5.21	0.84	0.18	-5.87	0.88
Mid-lat (30-60N/S)	0.35	-12.34	0.79	0.16	-5.39	0.86	0.06	-2.26	0.39	0.15	-4.90	0.83
High-lat (60-90N/S)	0.52	-18.15	0.92	0.16	-5.70	0.83	0.56	-19.25	0.78	0.17	-6.03	0.69
Pacific	0.41	-14.31	0.92	0.17	-5.65	0.88	0.07	-2.46	0.42	0.16	-5.25	0.84
Trop Pacific	0.29	-9.71	0.58	0.18	-5.93	0.87	0.16	-5.30	0.72	0.17	-5.66	0.84
S. Atlantic	0.38	-13.04	0.52	0.19	-6.30	0.91	0.18	-5.94	0.80	0.18	-6.21	0.86
N. Atlantic	0.21	-7.41	0.53	0.16	-5.42	0.84	0.16	-5.26	0.65	0.17	-5.75	0.82
Tropical Atlantic	0.16	-5.11	0.80	0.16	-5.29	0.81	0.13	-4.28	0.84	0.15	-4.74	0.81
Indian	0.16	-5.41	0.31	0.18	-6.00	0.88	0.19	-6.54	0.74	0.17	-5.63	0.85
Arctic	0.53	-18.21	0.92	0.15	-5.30	0.71	0.41	-14.95	0.62	0.14	-5.18	0.49
Southern Ocean	0.40	-13.94	0.70	0.07	-2.45	0.74	0.05	-1.81	0.08	0.08	-2.84	0.72

Table 2: Gradient (α^{SPACE}), intercept (δ_F) and r^2 values from least squares linear regressions on spatial sea surface salinity and δ_{Ow} data. Values are presented for observations (OBS) from the Global Seawater Oxygen-18 Database (Schmidt, 1999b; Bigg and Rohling, 2000, http://data.giss.nasa.gov/o18data/) and for the LH, LGM and LIG simulations. Observed values are biased to the spatial sampling coverage. Model values are calculated using all ocean grid points within each region and have been re-gridded to an equal area 100km grid.

opposing changes in mid and high-latitudes. During the LGM, α^{SPACE} decreases by >60% in the mid-latitudes and more than triples at high latitudes. The high latitude steepening of α^{SPACE} is concentrated in the Arctic in response to strongly depleted glacial precipitation and runoff, resulting in a reduced δ_F by $\sim$10 ‰. For many regions, the LGM yields the lowest r^2 values, suggesting that δ_{Ow} and salinity are most decoupled during glacial climate. There is almost no correlation between δ_{Ow} and salinity for the LGM Southern Ocean, when sea ice extent is largest and the signal-to-noise ratio becomes too low. Changes in α^{SPACE} between the LH and LIG are within $\pm$0.01 ‰/psu for all regions.

3.2.2. Temporal variability in paleosalinity reconstructions

The following section evaluates the temporal relationship between δ_{Ow} and salinity. Regional values of $\alpha^{DECADAL}$ and α^{SLICE} are presented in Table 3. Similar to Table 2, the gradient, intercept and r^2 values are presented from the least squares linear regression between decadal δ_{Ow} and salinity for each simulation and region. Correlations between decadal δ_{Ow} and salinity are much weaker than the spatial relationships. Regional values of α^{SPACE}, $\alpha^{DECADAL}$, and α^{SLICE} are compared for each simulation in Figure 3. For most regions, values of α^{SPACE} are steeper than $\alpha^{DECADAL}$, and α^{SLICE} values are steeper than α^{SPACE} and $\alpha^{DECADAL}$. Over large regions (eg. mid latitudes) the gradient between climates (α^{SLICE}) is relatively consistent with the LH spatial gradient (α^{SPACE}_{LH}), in agreement with results for the Pliocene presented by Tindall and Haywood (submitted). Figure 3

The spatial patterns of $\alpha^{DECADAL}$ and α^{SLICE}, calculated at each model grid point, are shown in Figures 4 and 5 respectively. $\alpha^{DECADAL}$ varies significantly across small spatial scales. The LGM $\alpha^{DECADAL}$ anomalies ($\alpha^{DECADAL}_{LGM-LH}$) are generally negative in the North Atlantic and positive in the Arctic. The North Atlantic anomalies coincide with changes in the location of the Gulf Stream in the west, and changes in the location of the polar front in the north-east. The LIG shows generally negative $\alpha^{DECADAL}$ anomalies ($\alpha^{DECADAL}_{LIG-LH}$) along the equator and positive anomalies in the latitude band of the Antarctic Circumpolar Current (ACC). The spatial pattern of α^{SLICE} differs from $\alpha^{DECADAL}$ for both the LGM and LIG (Figure 5). For most of the ocean, values of α^{SLICE} are steeper than $\alpha^{DECADAL}$. Exceptions to this are in the LIG equatorial Atlantic, where α^{SLICE}_{LIG-LH} is negative close to regions of small/negligible salinity change (masked areas in Figure 5), and in the glacial western Arctic, where α^{SLICE}_{LGM-LH} is also negative, suggesting that the δ_{Ow}-salinity signal is too small compared to the noise component in the system. Figure 4

Figure 6 presents the spatial and temporal δ_{Ow}-salinity relationships for a selection of ocean regions. Figure 5 The gradients differ significantly in a number of regions, such as the North Atlantic. During the LH, there

	LH			LGM			LIG			α^{SLICE}_{LGM-LH}	α^{SLICE}_{LIG-LH}
Region	$\alpha^{DECADAL}$	δ_F	r^2	$\alpha^{DECADAL}$	δ_F	r^2	$\alpha^{DECADAL}$	δ_F	r^2		
All Ocean	0.10	-3.45	0.54	0.18	-6.24	0.50	0.07	-2.31	0.83	0.41	0.42
Open Ocean	0.04	-1.28	0.03	0.13	-4.26	0.51	0.08	-2.59	0.89	0.19	2.05
Tropics (30N-30S)	0.07	-2.25	0.42	0.12	-3.95	0.44	0.05	-1.40	0.52	0.20	-0.39
Mid-lat (30-60N/S)	0.04	-2.03	0.11	0.10	-3.52	0.33	0.08	-2.62	0.74	0.18	0.14
High-lat (60-90N/S)	0.06	-2.45	0.34	0.28	-10.02	0.53	0.04	-1.67	0.38	-0.19	-2.37
Pacific	0.12	-3.95	0.86	0.20	-6.74	0.66	0.15	-5.04	0.82	0.17	0.31
Trop Pacific	0.12	-3.91	0.60	0.21	-6.87	0.74	0.21	-7.03	0.88	0.20	0.29
S. Atlantic	0.13	-4.42	0.82	0.18	-5.97	0.83	0.12	-4.14	0.76	0.19	0.27
N. Atlantic	0.07	-2.02	0.08	0.08	-2.56	0.56	0.07	-2.03	0.70	0.34	0.16
Tropical Atlantic	0.09	-2.80	0.47	0.07	-2.06	0.19	0.07	-2.16	0.62	0.27	-0.25
Indian	0.11	-3.68	0.71	0.14	-4.83	0.69	0.10	-3.44	0.92	0.09	0.13
Arctic	0.04	-2.03	0.11	0.39	-13.96	0.70	0.03	-1.63	0.31	-0.69	2.34
Southern Ocean	0.04	-1.55	0.45	0.07	-2.53	0.77	0.06	-2.15	0.73	0.04	0.16

Table 3: As Table 2 but for temporal relationships. Gradient ($\alpha^{DECADAL}$), intercept (δ_F) and r^2 values from least squares linear regressions on decadally averaged surface salinity and δ_{Ow} data from the last 100 years of each simulation. Regional α^{SLICE} values are also presented in the last two columns. Model values are calculated using all ocean grid points within each region.

is no significant relationship between decadal δ_{Ow} and salinity in the North Atlantic ($r^2 < 0.1$). Temporal gradients in the Southern Ocean remain <0.1 ‰/psu for all but the LIG-LH gradient. For most regions, the spatial gradient (α^{SPACE}) and the gradient between climates (α^{SLICE}) are steeper than each climate's intrinsic gradient ($\alpha^{DECADAL}$). Similar differences between the intrinsic and intra-simulation temporal gradients has been found for simulations covering the mid-Holocene and pre-industrial periods (Schmidt et al., 2007). Figure 6

The simulated salinity anomalies for the LGM and LIG and the magnitude of error in the estimated salinity using the δ_{Ow} residual method (applying the LH spatial δ_{Ow}-salinity gradients to simulated δ_{Ow} anomalies) are shown in Figure 7. The δ_{Ow} residual method captures the correct large-scale pattern in salinity anomalies in the mid and low-latitudes for both climates (Figure 7a-d). However, regional biases in the estimated salinity can exceed $\pm$4 psu for both the LGM and LIG (Figure 7e,f). The observed bias in the Mediterranean Sea will in part stem from the use of the open ocean δ_{Ow}-salinity gradient in this region, chosen due to the coarse resolution of the enclosed sea on the GCM grid. The agreement between spatial and temporal gradients may thus be improved if a Mediterranean specific gradient were applied. In the glacial Arctic, the estimated salinity change is of opposing sign to the actual simulated salinity anomaly. The difference between the estimated and actual salinity anomalies in the glacial northeast Atlantic and south of Greenland suggests that the actual salinity change may be larger than that inferred using the LH spatial gradients. Further south the estimated salinity anomalies overestimate the actual changes. For the LIG, estimated salinity anomalies are larger than the actual changes around the coast of Greenland, in the GIN seas, and in the Tropical Atlantic. Estimated salinity anomalies are slightly weaker than the actual change in the northern Indian Ocean. Across both climates, the error in the estimated salinity is generally smallest in the South Atlantic, Indian and Tropical Pacific Oceans. Figure 7

4. Discussion

4.1. Modelling insights for paleosalinity reconstruction

Our model simulations do not help characterise paleosalinity reconstruction uncertainties due to diagenetic errors, age uncertainties, species offsets or errors in the isolation of δ_{Ow} from δ_{Oc}. However, our simulations of the δ_{Ow}-salinity relationship across the entire globe can provide insight into the interpretation of unevenly distributed isotope data for paleosalinity reconstruction.

By comparing spatial and temporal relationships across regions it is possible to identify locations where paleosalinity reconstructions have low uncertainties and those with large uncertainties. Problem regions are the North Atlantic, Tropical Atlantic and high latitude regions, where a small signal-to-noise ratio produces low r^2 values between δ_{Ow} and salinity for one or more of the simulations. High latitude regions are clearly problematic for glacial-interglacial paleosalinity reconstructions, where the 'real' simulated δ_{Ow}-salinity relationship between climates (α^{SLICE}) is negative and the largest differences between spatial and temporal gradients are observed (Table 2 and Figure 3). During the LIG, the smallest difference between α^{SLICE} and each simulations multi-decadal δ_{Ow} and salinity co-variability ($\alpha^{DECADAL}$) are found in the Indian Ocean and the Tropical Pacific, where $\alpha^{DECADAL}$ is within 30 % of α^{SLICE}, suggesting good agreement in the δ_{Ow}-salinity relationship across temporal scales. For the LGM, the smallest differences are observed in the Tropical Pacific and South Atlantic, where $\alpha^{DECADAL}$ is within 10 % of α^{SLICE}. For both the LGM and LIG, $\alpha^{DECADAL}$ is only within 50 % of α^{SLICE} in the Tropical Pacific and within 55% in the South Atlantic, Indian and Pacific Oceans.

4.2. Physical controls on the δ_{Ow}-salinity relationship

Below we address why spatial and temporal δ_{Ow}-salinity gradients might not agree and discuss the sources of uncertainty in paleosalinity reconstruction, including how these may vary between glacial and interglacial climates.

4.2.1. Hydrological cycle

The coupling between δ_{Ow} and salinity generally observed in the global ocean suggests that the processes affecting both δ_{Ow} and salinity, such as regional E-P balance, dominate over processes which preferentially influence one variable over the other, such as a change in precipitation moisture source (Russon et al., 2013). However, these simulations show that changes in the distribution of insolation can produce feedbacks in the climate system that affect δ_{Ow} independently of salinity and thus complicate the interpretation of δ_{Ow}.

During the LIG, when no ice sheet changes have been applied, changes in the δ_{Ow}-salinity relationship are primarily driven by changes in the distribution of insolation. In this case, atmospheric water vapour pathways and conditions along an airmass trajectory are the fundamental cause of variability in δ_{Ow}-salinity relationships in the main ocean basins (LeGrande and Schmidt, 2011). Pathways of water exchange determine a region's freshwater end-member and any process that alters δ_F will lead to a changes in the δ_{Ow}-salinity relationship. Studies in the mid-latitudes and tropics have interpreted values of δ_F in terms of river discharge (Munksgaard et al., 2012), the isotopic composition of regional precipitation (δ_{Op}) (Benway and Mix, 2004; LeGrande and Schmidt, 2006; Abe et al., 2009), local evaporation regime (Conroy et al., 2014), and a mixture of evaporation, precipitation and runoff (Delaygue et al., 2001). Benway and Mix (2004) conclude that possible changes in the isotopic composition of freshwater budget terms is the largest source of error in paleosalinity reconstructions in the Panama Bight, estimating that a change in δ_{Op} of 3.5 ‰ would cause a 2 psu error in inferred salinity. This magnitude of change in δ_{Op} is well within the regional anomalies between our simulations.

The higher obliquity during the LIG and associated warmer northern hemisphere summer temperatures produces a reorganisation of the Intertropical Convergence Zone (ITCZ) and enriches δ_{Op} at high latitudes (thus enriching δ_F). These changes cause significant uncertainties in salinity reconstruction in the tropics and in the Arctic. Past salinity values determined from δ_{Ow} residuals alone may therefore require correcting for orbitally driven changes in atmospheric circulation in order to accurately isolate changes in E-P and thus the salinity signal, even during periods characterised by similar boundary conditions to today (LeGrande and Schmidt, 2009).

4.2.2. Ice-sheets and freezing processes

During glacial periods, changes in boundary conditions are larger and include the growth of ice sheets. Differences in δ_{Ow}-salinity relationships are thus larger as additional feedbacks, such as meltwater processes, add to the orbitally driven biases. This is the case for our LGM simulation, when the large northern hemisphere ice sheets cause large changes in the temporal δ_{Ow}-salinity gradient around its peripheries. The water stored in these ice sheets is highly depleted in δ_{Ow}. When this water reaches the surface ocean it depletes δ_F and significantly steepens the δ_{Ow}-salinity gradient (LeGrande and Schmidt, 2006; Schmidt et al., 2007).

The highly depleted freshwater from high-latitude ice sheets has been linked to instability in the oceanic thermohaline circulation and large changes in climate (Tindall and Valdes, 2011; LeGrande and Schmidt, 2008; Stouffer et al., 2007; Weaver et al., 2003). Miller et al. (2012) suggest that reduced basal melting around the fringes of the Antarctic ice sheet during the LGM may have played an important role in increasing the salinity of southern sourced waters. Changes in the freezing/melting regime around high latitude ice sheets can therefore significantly modify the δ_{Ow}-salinity relationship in the surrounding surface ocean and have globally reaching effects on deep ocean properties, through variable inputs of depleted freshwater and variable subsurface salt fluxes.

Decoupling of the δ_{Ow}-salinity relationship can also occur in the high latitude oceans due to changes in sea ice regime. Freezing processes result in salinity increases that are accompanied by essentially no observable change in seawater isotopic composition (Craig and Gordon, 1965; Lehmann and Siegenthaler, 1991; Pfirman et al., 2004) and therefore HadCM3 treats sea ice formation as non-fractionating. Consequently, melting and freezing have opposed (shallowing and steepening) effects on the δ_{Ow}-salinity gradient (Strain and Tan, 1993). The model visibly captures this effect in the response of α (e.g. Figure 4), however, we note that the approximate treatment of sea ice fractionation, as well as any imperfections in the model representation of sea ice, will introduce bias in the model results. Changes in the δ_{Ow}-salinity relationship invoked by sea ice formation are largely seasonal and not necessary reversible (Rohling and Bigg, 1998). Higher surface salinities from sea ice formation can initiate convection and mix surface waters with the ocean interior (e.g. Frew et al., 1995, 2000) or sea ice can be exported and subsequently melted in a new location. The δ_{Ow}-salinity relationship can thus become nonlinear (Rohling and Bigg, 1998; Strain and Tan, 1993). The effects of changing sea ice regime on the δ_{Ow}-salinity relationship can be seen around the coast of Antarctica and, more clearly, Greenland for both the LGM and LIG climate (Figure 7).

4.2.3. Ocean reorganisation

For periods with significant changes in boundary conditions (e.g. large ice sheets associated with glacial periods) ocean reorganisation can introduce large advective changes. Changes in the location of water mass boundaries or the position and magnitude of upwelling/downwelling fluxes will cause local salinity changes that may not reflect a change in the hydrological cycle. Additionally, because δ_{Ow} and salinity in subsurface waters behave conservatively (Paren and Potter, 1984; Frew et al., 1995), a change in oceanic source characteristics will not only affect the δ_{Ow}-salinity relationship of local seawater, but also in waters remote from the initial change (Rohling and Bigg, 1998). Thus Rohling and Bigg (1998) argue that the δ_{Ow}-salinity relationship in many regions is determined by advection rather than the local water balance.

Our simulations show the largest reorganisation of surface ocean currents during the LGM, when changes in orbit and ice volume increase the meridional temperature gradient. The North Atlantic in particular is a key region of interest for salinity and wider paleoceanographic reconstruction over the last glacial cycle due to its dynamic role in the global thermohaline circulation (CLIMAP Project Members, 1976; Pflaumann et al., 2003; Sarnthein et al., 2003; Broecker, 1989; MARGO Project Members, 2009). However, advective changes in the North Atlantic cause large uncertainties in the δ_{Ow}-salinity relationship. Consequently, during periods of significant climate change such as glacial-interglacial transitions, these results suggest that large salinity biases preclude traditional paleosalinity in locations of sharp gradients, unless it is concerned with reconstructing the past migration of oceanic fronts themselves or assessing large-scale patterns of change (Schmidt, 1999a; Caley and Roche, 2013).

5. Conclusion

We present isotope-enabled simulations using HadCM3 covering the Late Holocene, the Last Glacial Maximum and the Last Interglacial. A model-data comparison suggests that the model captures the general spatial pattern of planktonic δ_{Oc} during the Late Holocene and the Last Glacial Maximum, and we calculate a model 'best-fit' glacial enrichment of 1.08 ‰. The simulations are used to investigate how the relationship between surface ocean δ_{Ow} and salinity varies in response to past climate change. Modelled changes in δ_{Ow} are closely coupled to changes in the hydrological cycle and thus correlate with changes in salinity. However, our simulations show that the interpretation of δ_{Ow} as purely diagnosing changes in surface hydrology can be over-simplistic, especially on glacial-interglacial timescales.

Our results suggest that the relationship between δ_{Ow} and salinity can vary significantly over small spatial scales. This has implications when generalising a single value of α (the δ_{Ow}-salinity gradient) across large ocean regions, as is typically done for the δ_{Ow} residual method. Our results also suggest that the δ_{Ow}-salinity relationship has varied significantly through the past, i.e. δ_{Ow}-salinity spatial relationships do not necessarily equal δ_{Ow}-salinity temporal relationships. We show that spatial gradients are generally shallower but within $\sim$50 % of the actual simulated LH to LGM and LH to LIG temporal gradients. Temporal gradients calculated from each simulations multi-decadal variability are generally shallower than both spatial and actual simulated gradients.

Changes in sea ice regime, ocean circulation, and the isotopic terms in a regions freshwater budget clearly influence δ_{Ow} independent of salinity and can lead to uncertainties in salinity estimates exceeding $\pm$4 psu in regions that are sensitive to these processes. These results show that the relative importance of each control varies between glacial and interglacial climates. During the LIG, the different orbital configurations lead to changes in atmospheric moisture pathways and thus changes in regional δ_{Ow}-salinity relationships. During the LGM, larger changes in boundary conditions lead to significant sea ice and oceanic reorganisation, which add to salinity biases driven by orbital forcing alone.

Our simulations can help identify regions where spatial and temporal δ_{Ow}-salinity gradients overlap, providing some support to the classical method for reconstructing paleosalinity from δ_{Ow} in these locations. Our results suggest that the most robust paleosalinity reconstructions would be achieved in the South Atlantic, Tropical Pacific and Indian Oceans. Glacial-interglacial variability in the δ_{Ow}-salinity relationship is small in these regions.

These simulations suggest that reliable paleosalinity estimates cannot be derived in the North Atlantic or in high latitude regions. This is due to glacial-interglacial variability in the δ_{Ow}-salinity gradient. For these regions, additional constraints on the past freshwater budget or circulation, as well as multi-proxy approaches, may be necessary when attempting to reconstruct local salinity changes (e.g. Rohling, 2007; LeGrande and Schmidt, 2011).

Acknowledgements

This work was supported by NERC. MDH is supported on a NERC studentship tied between the British Antarctic Survey and the University of Bristol. JCT has received funding from the European Research Council under the European Union's Seventh Framework Programme (FP7/2007-2013)/ERC grant number 278636. Two anonymous reviewers are thanked for their constructive comments that helped improve the manuscript through the review process.

References

Abe, O., Agata, S., Morimoto, M., Abe, M., Yoshimura, K., Hiyama, T., Yoshida, N., 2009. A 6.5-year continuous record of sea surface salinity and seawater isotopic composition at Harbour of Ishigaki Island, southwest Japan. Isotopes in environmental and health studies 45 (3), 247–258.

Adkins, J. F., 2013. The role of deep ocean circulation in setting glacial climates. Paleoceanography 28 (3), 539–561. URL http://doi.wiley.com/10.1002/palo.20046

Adkins, J. F., Mcintyre, K., Schrag, D. P., 2002. The Salinity, Temperature, and δ18O of the Glacial Deep Ocean. Science 298, 1769–1773.

Annan, J. D., Hargreaves, J. C., 2013. A new global reconstruction of temperature changes at the Last Glacial Maximum. Climate of the Past 9, 367–376.

Benway, H. M., Mix, A. C., 2004. Oxygen isotopes, upper-ocean salinity, and precipitation sources in the eastern tropical Pacific. Earth and Planetary Science Letters 224 (3-4), 493–507. URL http://linkinghub.elsevier.com/retrieve/pii/S0012821X04003206

Berger, A., Loutre, M. F., 1991. Insolation values for the climate of the last 10 million years. Quaternary Science Reviews 10, 297–317.

Bigg, G., Rohling, E. J., 2000. An oxygen isotope data set for marine waters. Journal of Geophysical Research 105 (C4), 8527–8535.

Bingham, F. M., 2002. Sea surface salinity measurements in the historical database. Journal of Geophysical Research 107 (C12), 8019.
URL http://doi.wiley.com/10.1029/2000JC000767

Boyle, E., 2002. Oceanic Salt Switch. Science 298 (5599), 1724–1725.
URL http://www.sciencemag.org/content/298/5599/1724.short

Braconnot, P., Otto-Bliesner, B., Harrison, S., Joussaume, S., Peterchmitt, J.-Y., Abe-Ouchi, a., Crucifix, M., Driesschaert, E., Fichefet, T., Hewitt, C. D., Kageyama, M., Kitoh, a., Laîné, a., Loutre, M.-F., Marti, O., Merkel, U., Ramstein, G., Valdes, P., Weber, S. L., Yu, Y., Zhao, Y., 2007. Results of PMIP2 coupled simulations of the Mid-Holocene and Last Glacial Maximum âĂŞ Part 1: experiments and large-scale features. Climate of the Past 3 (2), 261–277.
URL http://www.clim-past.net/3/261/2007/

Broecker, W. S., 1989. The salinity contrast between the Atlantic and Pacific Oceans during glacial time. Paleoceanography 4 (2), 207–212.

Caley, T., Roche, D. M., 2013. δ18O water isotope in the iLOVECLIM model (version 1.0) âĂŞ Part 3: A palaeo-perspective based on present-day dataâĂŞmodel comparison for oxygen stable isotopes in carbonates. Geoscientific Model Development 6 (5), 1505–1516.
URL http://www.geosci-model-dev.net/6/1505/2013/

Caley, T., Roche, D. M., Waelbroeck, C., Michel, E., 2014. Oxygen stable isotopes during the Last Glacial Maximum climate: perspectives from dataâĂŞmodel (iLOVECLIM) comparison. Climate of the Past 10 (6), 1939–1955.
URL http://www.clim-past.net/10/1939/2014/cp-10-1939-2014.html

Capron, E., Govin, A., Stone, E. J., Masson-Delmotte, V., Mulitza, S., Otto-Bliesner, B., Rasmussen, T. L., Sime, L. C., Waelbroeck, C., Wolff, E. W., 2014. Temporal and spatial structure of multi-millennial temperature changes at high latitudes during the Last Interglacial. Quaternary Science Reviews 103, 116–133.
URL http://linkinghub.elsevier.com/retrieve/pii/S0277379114003382

Chappell, J., Shackleton, N. J., 1986. Oxygen isotopes and sea level. Nature 324 (6093), 137–140.

Clark, P. U., Dyke, A. S., Shakun, J. D., Carlson, A. E., Clark, J., Wohlfarth, B., Mitrovica, J. X., Hostetler, S. W., McCabe, a. M., 2009. The Last Glacial Maximum. Science 325 (5941), 710–4.
URL http://www.ncbi.nlm.nih.gov/pubmed/19661421

Conroy, J. L., Cobb, K. M., Lynch-stieglitz, J., Polissar, P. J., 2014. Constraints on the salinity âĂŞ oxygen isotope relationship in the central tropical Pacific Ocean. Marine Chemistry 161, 26–33.

Cox, M. D., 1984. A primitive equation, 3 dimensional model of the ocean. Tech. rep., GDFL Ocean Group.

Craig, H., Gordon, L., 1965. Deuterium and oxygen 18 variations in the ocean and the marine atmosphere. In: Tongiorgi, E. (Ed.), Stable Isotopes in Oceanographic Studies and Paleotemperatures. pp. 9–130.

Cutler, K., Edwards, R., Taylor, F., Cheng, H., Adkins, J., Gallup, C., Cutler, P., Burr, G., Bloom, A., 2003. Rapid sea-level fall and deep-ocean temperature change since the last interglacial period. Earth and Planetary Science Letters 206 (3-4), 253–271.
URL http://www.sciencedirect.com/science/article/pii/S0012821X0201107X

Delaygue, G., Bard, E., Rollion, C., Jouzel, J., Stiévenard, M., Duplessy, J.-C., 2001. Oxygen isotope/salinity relationship in the northern Indian Ocean. Journal of Geophysical Research 106 (C3), 4565–4574.

Delaygue, G., Jouzel, J., Dutay, J.-C., 2000. Oxygen 18-salinity relationship simulated by an oceanic general circulation model.

Earth and Planetary Science Letters 178 (1-2), 113–123.
URL http://linkinghub.elsevier.com/retrieve/pii/S0012821X0000073X

Duplessy, J. C., Bard, E., Labeyrie, L., Duprat, J., Moyes, J., 1993. Ocean isotope records and salinity changes in the northeastern Atlantic Ocean during the last 18,000 years. Paleoceanography 8 (3), 341–350.

Duplessy, J.-C., Labeyrie, L., Juillet-Leclerc, A., Maitre, F., Duprat, J., Sarnthein, M., 1991. Surface salinity reconstruction of the North Atlantic Ocean during the last glacial maximum. Oceanologica Acta 14 (4), 311–324.

Duplessy, J.-C., Labeyrie, L., Waelbroeck, C., 2002. Constraints on the ocean oxygen isotopic enrichment between the Last Glacial Maximum and the Holocene: Paleoceanographic implications. Quaternary Science Reviews 21 (1-3), 315–330.
URL http://www.sciencedirect.com/science/article/pii/S027737910100107X

Durack, P. J., Wijffels, S. E., Matear, R. J., 2012. Ocean salinities reveal strong global water cycle intensification during 1950 to 2000. Science 336 (6080), 455–8.
URL http://www.ncbi.nlm.nih.gov/pubmed/22539717

Dutton, A., Lambeck, K., 2012. Ice volume and sea level during the last interglacial. Science 337 (6091), 216–9.
URL http://www.ncbi.nlm.nih.gov/pubmed/22798610

Fairbanks, R., 1989. A 17,000-year glacio-eustatic seal level record: influence of glacial melting rates on the Younger Dryas event and deep-ocean circulation. Nature 342, 637–641.

Ferrari, R., Ferreira, D., 2011. What processes drive the ocean heat transport? Ocean Modelling 38 (3-4), 171–186.
URL http://www.sciencedirect.com/science/article/pii/S1463500311000485

Frew, R. D., Dennis, P. F., Heywood, K. J., Meredith, M. P., Boswell, S. M., 2000. The oxygen isotope composition of water masses in the northern North Atlantic. Deep Sea Research Part I: Oceanographic Research Papers 47 (12), 2265–2286.
URL http://www.sciencedirect.com/science/article/pii/S0967063700000236

Frew, R. D., Heywood, K. J., Dennis, P. F., 1995. Oxygen isotope study of water masses in the Princess Elizabeth Trough, Antarctica. Marine Chemistry 49 (2-3), 141–153.
URL http://www.sciencedirect.com/science/article/pii/030442039500003A

Furtado, J. C., Di Lorenzo, E., Cobb, K. M., Bracco, A., 2009. Paleoclimate Reconstructions of Tropical Sea Surface Temperatures from Precipitation Proxies: Methods, Uncertainties, and Nonstationarity. Journal of Climate 22 (5), 1104–1123.
URL http://dx.doi.org/10.1175/2008JCLI2415.1

Gordon, C., Cooper, C., Senior, C. A., Banks, H., Gregory, J. M., Johns, T. C., Wood, R. A., 2000. The simulation of SST, sea ice extents and ocean heat transports in a version of the Hadley Centre coupled model without flux adjustments. Climate Dynamics 16, 147–168.

Hennissen, J. A. I., Head, M. J., Schepper, S. D., Groeneveld, J., 2014. Palynological evidence for a southward shift of the North Atlantic Current at $\sim$2.6 Ma during the intensification of late Cenozoic Northern Hemisphere glaciation. Paleoceanography 29, 564–580.

Hewitt, C., Stouffer, R., Broccoli, A., Mitchell, J., Valdes, P., 2003. The effect of ocean dynamics in a coupled GCM simulation of the Last Glacial Maximum. Climate Dynamics 20 (2-3), 203–218.
URL http://dx.doi.org/10.1007/s00382-002-0272-6

Hut, G., 1987. Consultants' group meeting on stable isotope reference samples for geochemical and hydrological investigations. Report to the director general, International Atomic Energy Agency, Vienna.

IPCC, 2013. Climate Change 2013: The Physical Science Basis. Contribution of Working Group I to the Fifth Assessment Report of the Intergovernmental Panel on Climate Change. Cambridge University Press, Cambridge, United Kingdom and New York, NY, USA.

Jouzel, J., Vimeux, F., Caillon, N., Delaygue, G., Hoffmann, G., Masson-Delmotte, V., Parrenin, F., 2003. Magnitude of isotope/temperature scaling for interpretation of central Antarctic ice cores. Journal of Geophysical Research 108 (D12).
URL http://www.agu.org/pubs/crossref/2003/2002JD002677.shtml

Kopp, R. E., Simons, F. J., Mitrovica, J. X., Maloof, A. C., Oppenheimer, M., 2009. Probabilistic assessment of sea level during the last interglacial stage. Nature 462 (7275), 863–867.
URL http://www.ncbi.nlm.nih.gov/pubmed/20016591

Kopp, R. E., Simons, F. J., Mitrovica, J. X., Maloof, a. C., Oppenheimer, M., 2013. A probabilistic assessment of sea level variations within the last interglacial stage. Geophysical Journal International 193 (2), 711–716.
URL http://gji.oxfordjournals.org/cgi/doi/10.1093/gji/ggt029

Kukla, G. J., Bender, M. L., de Beaulieu, J.-L., Bond, G., Broecker, W. S., Cleveringa, P., Gavin, J. E., Herbert, T. D., Imbrie, J., Jouzel, J., Keigwin, L. D., Knudsen, K.-L., McManus, J. F., Merkt, J., Muhs, D. R., Müller, H., Poore, R. Z., Porter, S. C., Seret, G., Shackleton, N. J., Turner, C., Tzedakis, P. C., Winograd, I. J., 2002. Last Interglacial Climates. Quaternary Research 58 (1), 2–13.
URL http://linkinghub.elsevier.com/retrieve/pii/S0033589401923166

Labeyrie, L. D., Duplessy, J. C., Blanc, P. L., 1987. Variations in mode of formation and temperature of oceanic deep waters over the past 125,000 years. Nature 327, 477–482.

Leduc, G., Sachs, J. P., Kawka, O. E., Schneider, R. R., 2013. Holocene changes in eastern equatorial Atlantic salinity as estimated by water isotopologues. Earth and Planetary Science Letters 362, 151–162.
URL http://linkinghub.elsevier.com/retrieve/pii/S0012821X12006887

Lee, J.-E., Fung, I., DePaolo, D. J., Henning, C. C., 2007. Analysis of the global distribution of water isotopes using the NCAR atmospheric general circulation model. Journal of Geophysical Research 112.
URL http://www.agu.org/pubs/crossref/2007/2006JD007657.shtml

Lee, J.-E., Fung, I., DePaolo, D. J., Otto-Bliesner, B., 2008. Water isotopes during the Last Glacial Maximum: New general circulation model calculations. Journal of Geophysical Research 113, 15pp.
URL http://www.agu.org/pubs/crossref/2008/2008JD009859.shtml

LeGrande, A. N., Schmidt, G. A., 2006. Global gridded data set of the oxygen isotopic composition in seawater. Geophysical Research Letters 33 (12), L12604.
URL http://doi.wiley.com/10.1029/2006GL026011

LeGrande, A. N., Schmidt, G. A., 2008. Ensemble, water isotope-enabled, coupled general circulation modeling insights into the 8.2 ka event. Paleoceanography 23 (3).
URL http://doi.wiley.com/10.1029/2008PA001610

LeGrande, A. N., Schmidt, G. A., 2009. Sources of Holocene variability of oxygen isotopes in paleoclimate archives. Climate of the Past 5, 441–455.

LeGrande, A. N., Schmidt, G. A., 2011. Water isotopologues as a quantitative paleosalinity proxy. Paleoceanography 26 (3).
URL http://doi.wiley.com/10.1029/2010PA002043

Lehmann, M., Siegenthaler, U., 1991. Equilibrium oxygen-and hydrogen-isotope fractionation between ice and water. Journal of Glaciology 37 (125), 23–26.
URL http://www.igsoc.org:8080/journal/37/125/igs_journal_vol37_issue125_pg23-26.pdf

Loulergue, L., Schilt, A., Spahni, R., Masson-Delmotte, V., Blunier, T., Lemieux, B., Barnola, J.-M., Raynaud, D., Stocker, T. F., Chappellaz, J., 2008. Orbital and millennial-scale features of atmospheric CH4 over the past 800,000 years. Nature 453 (7193), 383–6.
URL http://www.ncbi.nlm.nih.gov/pubmed/18480822

Lynch-Stieglitz, J., Curry, W. B., Slowey, N., 1999. Weaker Gulf Stream in the Florida Straits during the Last Glacial Maximum. Nature 402 (6762), 644–648.
URL http://dx.doi.org/10.1038/45204

Masson-Delmotte, V., Braconnot, P., Hoffmann, G., Jouzel, J., Kageyama, M., Landais, A., Lejeune, Q., Risi, C., Sime, L., Sjolte, J., Swingedouw, D., Vinther, B., 2011. Sensitivity of interglacial Greenland temperature and δ18O: ice core data, orbital and increased CO2 climate simulations. Climate of the Past 7, 1041–1059.
URL http://www.clim-past.net/7/1041/2011/

Masson-Delmotte, V., Hou, S., Ekaykin, A., Jouzel, J., Aristarain, A., Bernardo, R. T., Bromwich, D., Cattani, O., Delmotte, M., Falourd, S., Frezzotti, M., Gallée, H., Genoni, L., Isaksson, E., Landais, A., Helsen, M. M., Hoffmann, G., Lopez, J., Morgan, V., Motoyama, H., Noone, D., Oerter, H., Petit, J. R., Royer, A., Uemura, R., Schmidt, G. a., Schlosser, E., Simões, J. C., Steig, E. J., Stenni, B., Stievenard, M., van den Broeke, M. R., van de Wal, R. S. W., van de Berg, W. J., Vimeux, F., White, J. W. C., 2008. A Review of Antarctic Surface Snow Isotopic Composition: Observations, Atmospheric Circulation, and Isotopic Modeling. Journal of Climate 21, 3359–3387.
URL http://journals.ametsoc.org/doi/abs/10.1175/2007JCLI2139.1

McConnell, M. C., Thunell, R. C., Lorenzoni, L., Astor, Y., Wright, J. D., Fairbanks, R., 2009. Seasonal variability in the salinity and oxygen isotopic composition of seawater from the Cariaco Basin, Venezuela: Implications for paleosalinity reconstructions. Geochemistry, Geophysics, Geosystems 10 (6).
URL http://doi.wiley.com/10.1029/2008GC002035

Miller, M. D., Adkins, J. F., Menemenlis, D., Schodlok, M. P., 2012. The role of ocean cooling in setting glacial southern source bottom water salinity. Paleoceanography 27 (3).
URL http://doi.wiley.com/10.1029/2012PA002297

Munk, W., Wunsch, C., 1998. Abyssal recipes II: energetics of tidal and wind mixing. Deep Sea Research Part I: Oceanographic Research Papers 45 (12), 1977–2010.
URL http://linkinghub.elsevier.com/retrieve/pii/S0967063798000703

Munksgaard, N. C., Wurster, C. M., Bass, A., Zagorskis, I., Bird, M. I., 2012. First continuous shipboard δ18O and δD measurements in sea water by diffusion sampling-cavity ring-down spectrometry. Environmental Chemistry Letters 10 (3), 301–307.
URL http://link.springer.com/10.1007/s10311-012-0371-5

Noone, D., Simmonds, I., 2002. Associations between δ18O of Water and Climate Parameters in a Simulation of Atmospheric Circulation for 1979-95. Journal of Climate 15, 3150–3169.

CLIMAP Project Members, 1976. The Surface of the Ice-Age Earth. Science 191 (4232), 1131–1137.
URL http://www.sciencemag.org/content/191/4232/1131.abstract

MARGO Project Members, 2009. Constraints on the magnitude and patterns of ocean cooling at the Last Glacial Maximum. Nature Geoscience 2 (2), 127–132.
URL http://dx.doi.org/10.1038/ngeo411

O'Neil, J. R., Clayton, R. N., Mayeda, T. K., 1969. Oxygen Isotope Fractionation in Divalent Metal Carbonates. The Journal of Chemical Physics 51 (12), 5547.
URL http://scitation.aip.org/content/aip/journal/jcp/51/12/10.1063/1.1671982

Pardaens, a. K., Banks, H. T., Gregory, J. M., Rowntree, P. R., 2003. Freshwater transports in HadCM3. Climate Dynamics 21 (2), 177–195.
URL http://link.springer.com/10.1007/s00382-003-0324-6

Paren, J. G., Potter, J. R., 1984. Isotopic tracers in polar seas and glacier ice. Journal of Geophysical Research: Oceans 89 (C1), 749–750.
URL http://dx.doi.org/10.1029/JC089iC01p00749

Peltier, W. R., 2004. Global glacial isostasy and the suraface of the ice-age Earth: The ICE-5G (VM2) Model and GRACE. Annual Review of Earth and Planetary Sciences 32, 111–149.
URL http://dx.doi.org/10.1146/annurev.earth.32.082503.144359

Petit, J. R., Raynaud, D., Basile, I., Chappellaz, J., Davisk, M., Ritz, C., Delmotte, M., Legrand, M., Lorius, C., Pe, L., Saltzmank, E., 1999. Climate and atmospheric history of the past 420,000 years from the Vostok ice core, Antarctica. Nature 399, 429–436.

Pfirman, S., Haxby, W., Eicken, H., Jeffries, M., Bauch, D., 2004. Drifting Arctic sea ice archives changes in ocean surface conditions. Geophysical Research Letters 31 (19).

Pflaumann, U., Sarnthein, M., Chapman, M., D'Abreu, L., Funnell, B., Huels, M., Kiefer, T., Maslin, M., Schulz, H., Swallow, J., van Kreveld, S., Vautravers, M., Vogelsang, E., Weinelt, M., 2003. Glacial North Atlantic: Sea-surface conditions reconstructed by GLAMAP 2000. Paleoceanography 18 (3), 1065.
URL http://dx.doi.org/10.1029/2002PA000774

Roche, D., Paillard, D., Ganopolski, A., Hoffmann, G., 2004. Oceanic oxygen-18 at the present day and LGM: equilibrium simulations with a coupled climate model of intermediate complexity. Earth and Planetary Science Letters 218 (3-4), 317–330.
URL http://www.sciencedirect.com/science/article/pii/S0012821X03007003

Rohling, E., Bigg, G., 1998. Paleosalinity and δ18O: A critical assessment. Journal of Geophysical Research 103 (C1), 1307–1318.

Rohling, E. J., 2000. Paleosalinity: confidence limits and future applications. Marine Geology 163 (1-4), 1–11.
URL http://linkinghub.elsevier.com/retrieve/pii/S0025322799000973

Rohling, E. J., 2007. Progress in paleosalinity: Overview and presentation of a new approach. Paleoceanography 22 (3).
URL http://doi.wiley.com/10.1029/2007PA001437

Rostek, F., Ruhland, G., Bassinot, F., Müller, P., Labeyrie, L., Lancelot, Y., Bard, E., 1993. Reconstructing sea surface temperature and salinity using δ18O and alkenone records. Nature 364, 319–321.

Ruddiman, W. F., Cline, R. M. L., Hays, J. D., Prell, W. L., Moore, T. C., Kipp, N. G., Molfino, B. E., Denton, G. H., Hughes, T. J., Balsam, W. L., Brunner, C. A., Duplessy, J.-C., Fastook, J. L., Imbrie, J., Keigwin, L. D., Kellogg, T. B., McIntyre, A., Matthews, R. K., Mix, A. C., Morley, J. J., Shackleton, N. J., Streeter, S., Thompson, P. R., 1984. The last interglacial ocean. Quaternary Research 21 (2), 123–224.
URL http://www.sciencedirect.com/science/article/pii/003358948490098X

Russon, T., Tudhope, a. W., Hegerl, G. C., Collins, M., Tindall, J., 2013. Inter-annual tropical Pacific climate variability in an isotope-enabled CGCM: implications for interpreting coral stable oxygen isotope records of ENSO. Climate of the Past 9 (4), 1543–1557.
URL http://www.clim-past.net/9/1543/2013/

Sarnthein, M., Gersonde, R., Niebler, S., Pflaumann, U., Spielhagen, R., Thiede, J., Wefer, G., Weinelt, M., 2003. Overview of Glacial Atlantic Ocean Mapping (GLAMAP 2000). Paleoceanography 18 (2), 1030.
URL http://dx.doi.org/10.1029/2002PA000769

Schmidt, G. A., 1999a. Error analysis of paleosalinity calculations. Paleoceanography 14, 422–429.

Schmidt, G. A., 1999b. Forward modeling of carbonate proxy data from planktonic foraminifera using oxygen isotope tracers in a global ocean model. Paleoceanography 14 (4), 482–497.

Schmidt, G. A., LeGrande, A. N., Hoffmann, G., 2007. Water isotope expressions of intrinsic and forced variability in a coupled ocean-atmosphere model. Journal of Geophysical Research 112.
URL http://www.agu.org/pubs/crossref/2007/2006JD007781.shtml

Schmidt, G. A., Mulitza, S., 2002. Global calibration of ecological models for planktic foraminifera from coretop carbonate oxygen-18. Marine Micropaleontology 44 (3-4), 125–140.

Schrag, D. P., Adkins, J. F., McIntyre, K., Alexander, J. L., Hodell, D. a., Charles, C. D., McManus, J. F., 2002. The oxygen isotopic composition of seawater during the Last Glacial Maximum. Quaternary Science Reviews 21 (1-3), 331–342.
URL http://linkinghub.elsevier.com/retrieve/pii/S027737910100110X

Schrag, D. P., Hampt, G., Murray, D. W., 1996. Pore fluid constraints on the temperature and oxygen isotopic composition of the glacial ocean. Science 272 (5270), 1930–1932.

Shackleton, N., 1987. Oxygen isotopes, ice volume and sea level. Quaternary Science Reviews 6 (3-4), 183–190.
URL http://www.sciencedirect.com/science/article/pii/0277379187900035

Shackleton, N. J., 1967. Oxygen Isotope Analyses and Pleistocene Temperatures Re-assessed. Nature 215 (5096), 15–17.
URL http://dx.doi.org/10.1038/215015a0

Shackleton, N. J., 1974. Attainment of isotopic equillibrium between ocean water and the benthic foraminifera Genus Uvigerina: Isotopic changes in the ocean during the Last Glacial. Colloques Internationaux du C.N.R.S. 219, 203–209.

Shackleton, N. J., Chapman, M., Sánchez-Goñi, M. F., Pailler, D., Lancelot, Y., 2002. The Classic Marine Isotope Substage 5e. Quaternary Research 58 (1), 14–16.
URL http://linkinghub.elsevier.com/retrieve/pii/S0033589401923129

Sima, A., Paul, A., Schulz, M., Oerlemans, J., 2006. Modeling the oxygen-isotopic composition of the North American Ice Sheet and its effect on the isotopic composition of the ocean during the last glacial cycle. Geophysical Research Letters 33 (15), L15706.
URL http://dx.doi.org/10.1029/2006GL026923

Sime, L. C., Risi, C., Tindall, J. C., Sjolte, J., Wolff, E. W., Masson-delmotte, V., Capron, E., 2013. Warm climate isotopic simulations: what do we learn about interglacial signals in Greenland ice cores? Quaternary Science Reviews 67, 59–80.

Sime, L. C., Tindall, J. C., Wolff, E. W., Connolley, W. M., Valdes, P. J., 2008. Antarctic isotopic thermometer during a CO2 forced warming event. Journal of Geophysical Research 113.
URL http://www.agu.org/pubs/crossref/2008/2008JD010395.shtml

Sime, L. C., Wolff, E. W., Oliver, K. I. C., Tindall, J. C., 2009. Evidence for warmer interglacials in East Antarctic ice cores. Nature 462, 342–345.
URL http://www.ncbi.nlm.nih.gov/pubmed/19924212

Singarayer, J. S., Valdes, P. J., 2010. High-latitude climate sensitivity to ice-sheet forcing over the last 120kyr. Quaternary Science Reviews 29 (1-2), 43–55.
URL http://linkinghub.elsevier.com/retrieve/pii/S0277379109003564

Solomon, S., Qin, D., Manning, M., Alley, R., Berntsen, T., Bindoff, N., Chen, Z., Chidthaisong, A., Gregory, J., Hegerl, G., Heimann, M., Hewitson, B., Hoskins, B., Joos, F., Jouzel, J., Kattsov, V., Lohmann, U., Matsuno, T., Molina, M., Nicholls, N., Overpeck, J., Raga, G., Ramaswamy, V., Ren, J., Rusticucci, M., Somerville, R., Stocker, T., Whetton, P., Wood, R., Wratt, D., 2007. Climate Change 2007: The Physical Science Basis. Contribution of Working Group I to the Fourth Assessment Report of the Intergovernmental Panel on Climate Change. Cambridge University Press.
URL http://ipcc-wg1.ucar.edu/ wg1/wg1-report.html

Spahni, R., Chappellaz, J., Stocker, T. F., Loulergue, L., Hausammann, G., Kawamura, K., Flückiger, J., Schwander, J., Raynaud, D., Masson-Delmotte, V., Jouzel, J., 2005. Atmospheric Methane and Nitrous Oxide of the Late Pleistocene from Antarctic Ice Cores. Science 310 (5752), 1317–1321.
URL http://www.sciencemag.org/content/310/5752/1317.abstract

Stott, L., Cannariato, K., Thunell, R., Haug, G. H., Koutavas, A., Lund, S., 2004. Decline of surface temperature and salinity in the western tropical Pacific Ocean in the Holocene epoch. Nature 431, 2–5.

Stouffer, R., Seidov, D., Haupt, B., 2007. Climate Response to External Sources of Freshwater: North Atlantic versus the Southern Ocean. Journal of Climate 20, 436–448.

Strain, P. M., Tan, F. C., 1993. Seasonal evolution of oxygen isotope-salinity relationships in high-latitude surface waters. Journal of Geophysical Research: Oceans 98 (C8), 14589–14598.
URL http://dx.doi.org/10.1029/93JC01182

Thresher, D. E., 2004. Multi-Century Simulations of LGM and Present Day Climate Using an Accelerated Coupled GCM Carrying Water Isotope Tracers, With Comparisons to Ocean Sediment/Ice Cores and Observations. Phd thesis, Columbia University.

Tindall, J., Flecker, R., Valdes, P., Schmidt, D. N., Markwick, P., Harris, J., 2010. Modelling the oxygen isotope distribution of ancient seawater using a coupled ocean-atmosphere GCM: Implications for reconstructing early Eocene climate. Earth and Planetary Science Letters 292 (3-4), 265–273.
URL http://linkinghub.elsevier.com/retrieve/pii/S0012821X10000130

Tindall, J., Haywood, A., submitted. Modeling Oxygen Isotopes in the Pliocene: Large Scale Features over the Land and Ocean. Paleoceanography.

Tindall, J. C., Valdes, P. J., 2011. Modeling the 8.2 ka event using a coupled atmosphere-ocean GCM. Global and Planetary Change 79, 312–321.
URL http://linkinghub.elsevier.com/retrieve/pii/S0921818111000312

Tindall, J. C., Valdes, P. J., Sime, L. C., 2009. Stable water isotopes in HadCM3: Isotopic signature of El Niño-Southern Oscillation and the tropical amount effect. Journal of Geophysical Research 114, 12pp.
URL http://www.agu.org/pubs/crossref/2009/2008JD010825.shtml

Turney, C. S. M., Jones, R. T., 2010. Does the Agulhas Current amplify global temperatures during super-interglacials? Journal of

Quaternary Science 25 (6), 839–843.
URL http://dx.doi.org/10.1002/jqs.1423

Waelbroeck, C., Kiefer, T., Dokken, T., Chen, M.-T., Spero, H., Jung, S., Weinelt, M., Kucera, M., Paul, a., 2014. Constraints on surface seawater oxygen isotope change between the Last Glacial Maximum and the Late Holocene. Quaternary Science Reviews 105, 102–111.
URL http://linkinghub.elsevier.com/retrieve/pii/S0277379114003680

Waelbroeck, C., Mulitza, S., Spero, H., Dokken, T., Kiefer, T., Cortijo, E., 2005. A global compilation of late Holocene planktonic foraminiferal δ18O: relationship between surface water temperature and δ18O. Quaternary Science Reviews 24 (7-9), 853–868.
URL http://linkinghub.elsevier.com/retrieve/pii/S0277379104002197

Weaver, A. J., Saenko, O. A., Clark, P. U., Mitrovica, J. X., 2003. Meltwater pulse 1A from Antarctica as a trigger of the Bølling-Allerød warm interval. Science 299 (5613), 1709–13.
URL http://www.ncbi.nlm.nih.gov/pubmed/12637739

Weldeab, S., 2012. Bipolar modulation of millennial-scale West African monsoon variability during the last glacial (75,000-25,000 years ago). Quaternary Science Reviews 40, 21–29.
URL http://linkinghub.elsevier.com/retrieve/pii/S0277379112000959

Werner, M., Langebroek, P. M., Carlsen, T., Herold, M., 2011. Stable water isotopes in the ECHAM5 general circulation model: Toward high-resolution isotope modeling on a global scale. Journal of Geophysical Research 116, 14pp.

Wunsch, C., 2002. What Is the Thermohaline Circulation? Science 298 (5596), 1179–1181.
URL http://www.sciencemag.org/content/298/5596/1179.short

Xinping, Z., Zhian, S., Huade, G., Xinzhu, Z., Huawu, W., Yimin, H., 2012. GCM Simulations of Stable Isotopes in the Water Cycle in Comparison with GNIP Observations over East Asia. Acta Meteorologica Sinica 26 (2011001), 420–437.

Tables

Exp	Orbit ka	CO_2 ppmv	CH_4 ppmv	N_2O ppmv	Orography ka
LH	0	280	0.76	0.27	0
LGM	21	186	0.37	0.25	21
LIG	125	275	0.64	0.26	0

Table 1: List of isotope-enabled HadCM3 simulations and prescribed boundary conditions. We adopt the same boundary forcing as applied by Singarayer and Valdes (2010): orbital parameters are taken from Berger and Loutre (1991); atmospheric CO_2 is derived from the Vostok ice core (Petit et al., 1999; Loulergue et al., 2008); and CH_4 and N_2O from the EPICA Dome-C ice core (Spahni et al., 2005).

Figure Captions

Figure 1. Modelled surface ocean δ_{Oc}, calculated from the equation of Shackleton (1974). Superimposed coloured dots represent individual planktonic foraminifera calcite δ_{Oc} data. Model and data for the LH (top left), LGM (middle left), and LIG (bottom left). The LGM-LH δ_{Oc} anomaly, with a 1.0 ‰ glacial enrichment subtracted from the data (middle right), and LIG-LH δ_{Oc} anomaly (bottom right). Data for the Late Holocene is from the Waelbroeck et al. (2005) dataset, defined as 0-4 ka, and LGM anomalies are from the compilation of Caley et al. (2014), with the LGM defined as 19-23 ka and LH as 0-3 ka.

Figure 2. Regional relationships between spatial sea surface salinity and δ_{Ow} for a selection of ocean regions. Top left panel shows all observations from the GISS Global Seawater Oxygen-18 Database (Schmidt, 1999b; Bigg and Rohling, 2000, http://data.giss.nasa.gov/o18data/), coloured by degrees latitude. Subsequent panels show individual observations in black. All model grid points within each region are shown in orange, after being re-gridded to an equal area 100km grid. The modelled values taken from the closest ocean grid point to each observed value are shown in red. The least squares linear regression for observed data (Obs), all model grid points within each region on an equal area grid (All Mod) and the model grid points where observations are available (Mod) are also shown.

Figure 3. Comparison of spatial and temporal δ_{Ow}-salinity gradients; α^{SPACE} (the relative co-variability of δ_{Ow} and salinity over a region), $\alpha^{DECADAL}$ (the decadal co-variability of δ_{Ow} and salinity at a given point in space), and α^{SLICE} (the actual relationship between δ_{Ow} and salinity between the Last Glacial Maximum and Late Holocene [LGM-LH] or Last Interglacial and Late Holocene [LIG-LH] at a given point in space). Top panels show the LGM gradients as filled triangles (far left panel also shows LH gradients as filled circles). Bottom panels show the LIG gradients as filled squares. Left panels: difference between α^{SPACE} and $\alpha^{DECADAL}$ for each ocean region, representing the difference between the δ_{Ow} residual method, based on modern spatial gradients, and decadal δ_{Ow}-salinity co-variability. Middle panels: as left but between α^{SPACE} and α^{SLICE}, representing the comparison between the δ_{Ow} residual method and the actual modelled δ_{Ow}-salinity gradient. Right panels: as left and middle but between $\alpha^{DECADAL}$ and α^{SLICE}. Regional values of α^{SLICE} for the LGM-LH and LIG-LH that lie outside the axis limits on the middle and right panel are

quoted below the figure. Filled colours denote each region that the gradient has been averaged over and are shown in the legend on the far right. The one-to-one line, representing perfect agreement between gradients, is also plotted (black dashed line).

Figure 4. Multi-decadal co-variability of salinity and δ_{Ow} at each model grid point. Top: Gradient of the local linear regression on multi-decadal variability between sea surface salinity and sea surface δ_{Ow} over the last 100 years of the LH simulation ($\alpha_{LH}^{DECADAL}$). Middle: Difference in $\alpha^{DECADAL}$ between the LGM and LH simulations ($\alpha_{LGM-LH}^{DECADAL}$). Bottom: Difference in $\alpha^{DECADAL}$ between the LIG and LH simulations ($\alpha_{LIG-LH}^{DECADAL}$).

Figure 5. Modelled temporal δ_{Ow}-salinity gradient (α^{SLICE}) between the LGM and LH (top; α_{LGM-LH}^{SLICE}) and LIG and LH (bottom; α_{LIG-LH}^{SLICE}). Regions are masked where the change in salinity is small using a threshold of 0.1σ for the LGM-LH (0.24 psu) and 0.14σ for the LIG-LH (0.11 psu). A filled black circle, triangle, and square represent the locations plotted in the left, middle and right panels of Figure S3 respectively (see Supplementary Information).

Figure 6. Variability between δ_{Ow}-salinity gradients across selected ocean regions. Filled circles represent decadally averaged δ_{Ow} and salinity values for the LH (black), LGM (blue) and LIG (red). Filled squares represent average δ_{Ow} and salinity values calculated over the final 100 years of the LH (green), LGM (mauve) and LIG (orange) simulations. Lines show the linear relationships between multi-decadal data (solid lines), centennially averaged data (dashed lines), and spatially averaged data (light grey, light blue and light red for LH, LGM, and LIG respectively, dot-dashed lines). The values of α^{SPACE}, $\alpha^{DECADAL}$, and α^{SLICE} are also shown on the figure with the associated r^2 values for $\alpha^{DECADAL}$ and α^{SPACE}.

Figure 7. The δ_{Ow} residual method. Top panels: Salinity anomalies between a) the LGM-LH and b) the LIG-LH. Middle panels: Inferred salinity anomalies using the δ_{Ow} residual method for c) the LGM and d) the LIG (calculated by applying the LH spatial slopes to the LGM-LH and LIG-LH δ_{Ow} anomalies respectively). Bottom panels show the difference between the modelled salinity anomalies (top panels) and inferred salinity anomalies using the δ_{Ow} residual method (middle panels) for e) the LGM-LH and f) the LIG-LH. For subplots c-f, spatial slopes are calculated regionally over the North Atlantic, South Atlantic, Tropical Atlantic, extratropical Pacific, Tropical Pacific, Indian, Southern and Arctic Ocean (see

Supplementary Information). Estimated salinity anomalies for areas of the surface ocean outside these regional definitions and in marginal seas were calculated using the open ocean spatial slope.

Figures

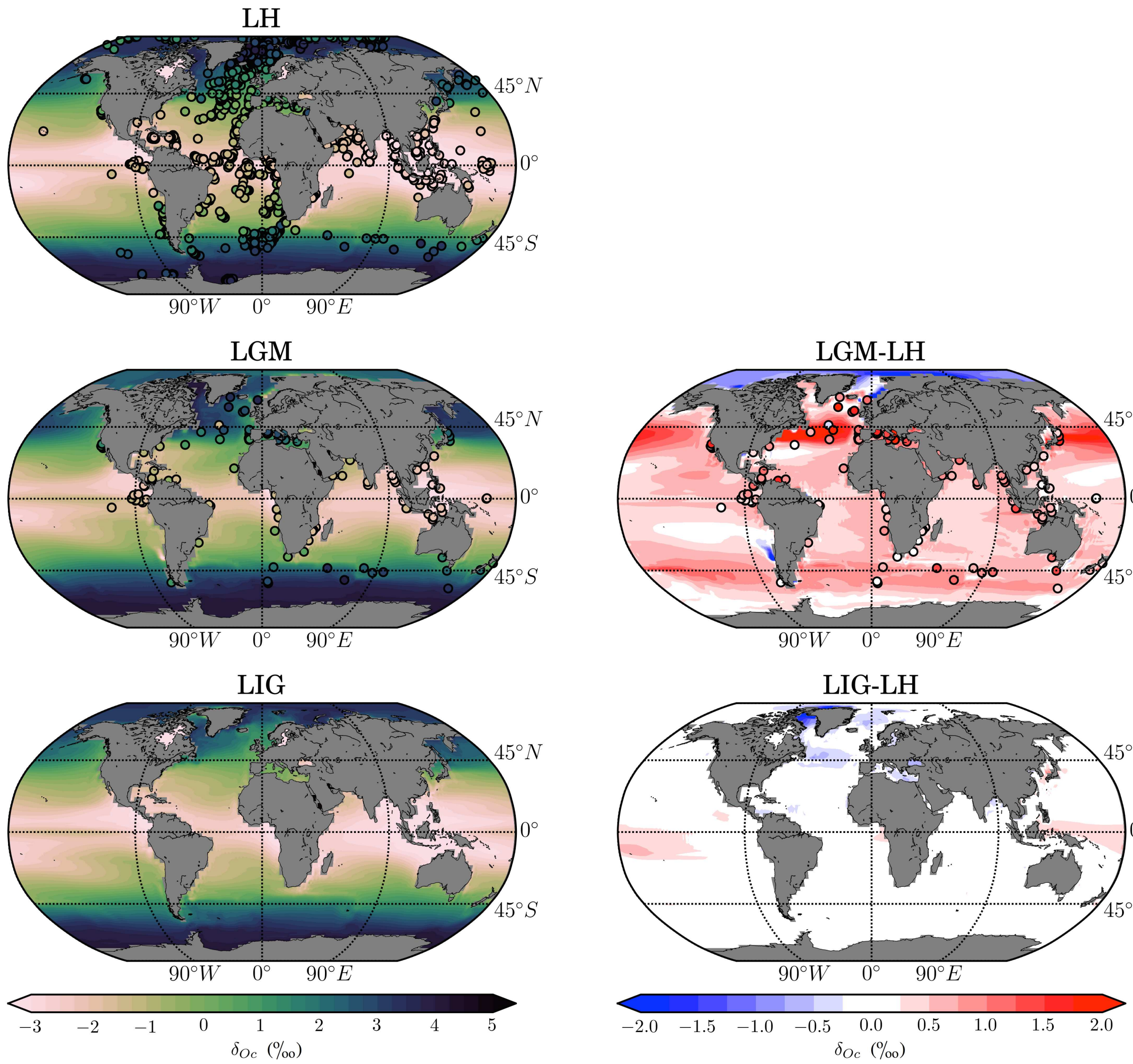

Figure 1: Modelled surface ocean δ_{Oc}, calculated from the equation of Shackleton (1974). Superimposed coloured dots represent individual planktonic foraminifera calcite δ_{Oc} data. Model and data for the LH (top left), LGM (middle left), and LIG (bottom left). The LGM-LH δ_{Oc} anomaly, with a 1.0 ‰ glacial enrichment subtracted from the data (middle right), and LIG-LH δ_{Oc} anomaly (bottom right). Data for the Late Holocene is from the Waelbroeck et al. (2005) dataset, defined as 0-4 ka, and LGM anomalies are from the compilation of Caley et al. (2014), with the LGM defined as 19-23 ka and LH as 0-3 ka.

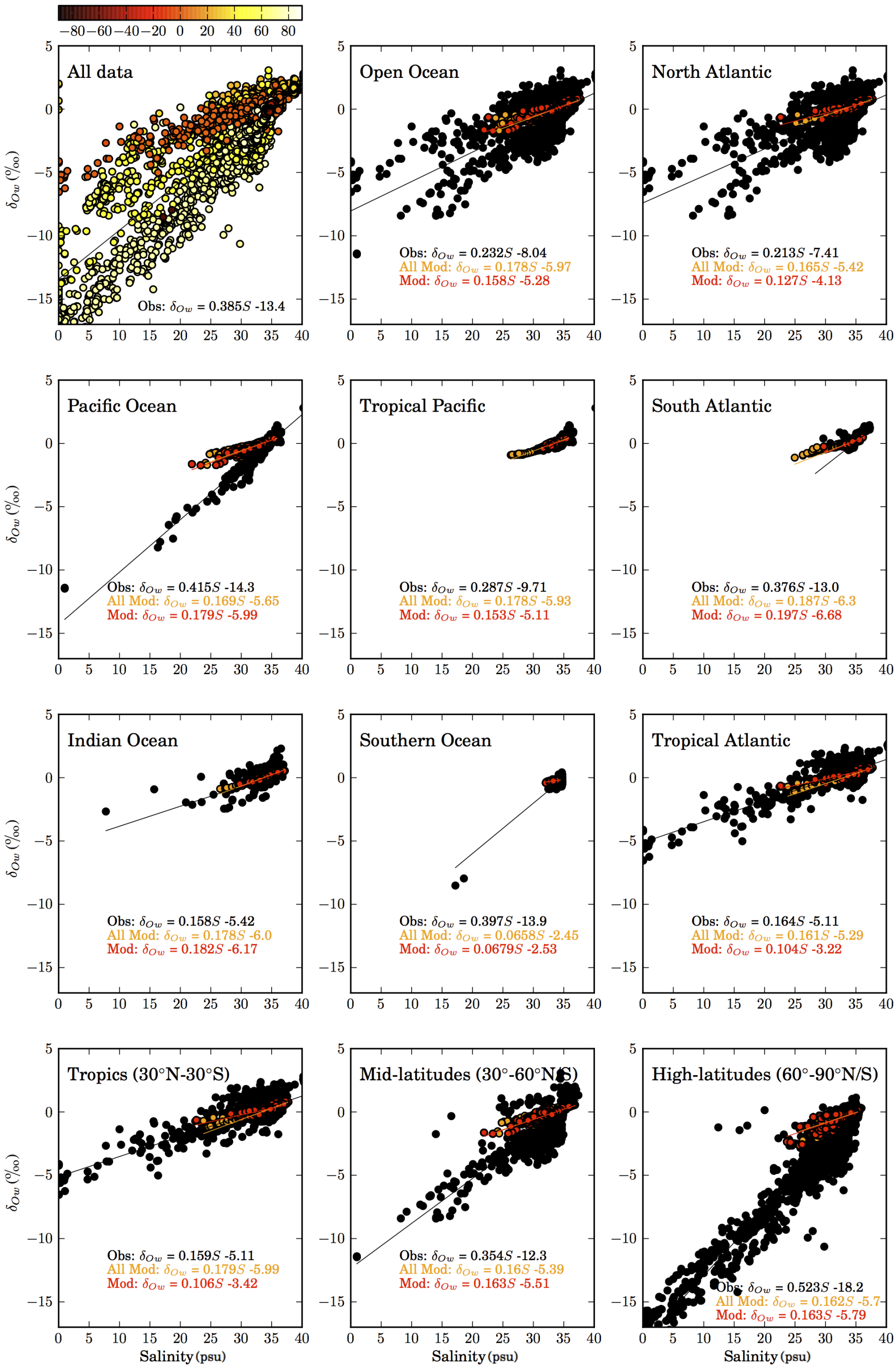

Figure 2: Regional relationships between spatial sea surface salinity and δ_{Ow} for a selection of ocean regions. Top left panel shows all observations from the GISS Global Seawater Oxygen-18 Database (Schmidt, 1999b; Bigg and Rohling, 2000, http://data.giss.nasa.gov/o18data/), coloured by degrees latitude. Subsequent panels show individual observations in black. All model grid points within each region are shown in orange, after being re-gridded to an equal area 100km grid. The modelled values taken from the closest ocean grid point to each observed value are shown in red. The least squares linear regression for observed data (Obs), all model grid points within each region on an equal area grid (All Mod) and the model grid points where observations are available (Mod) are also shown.

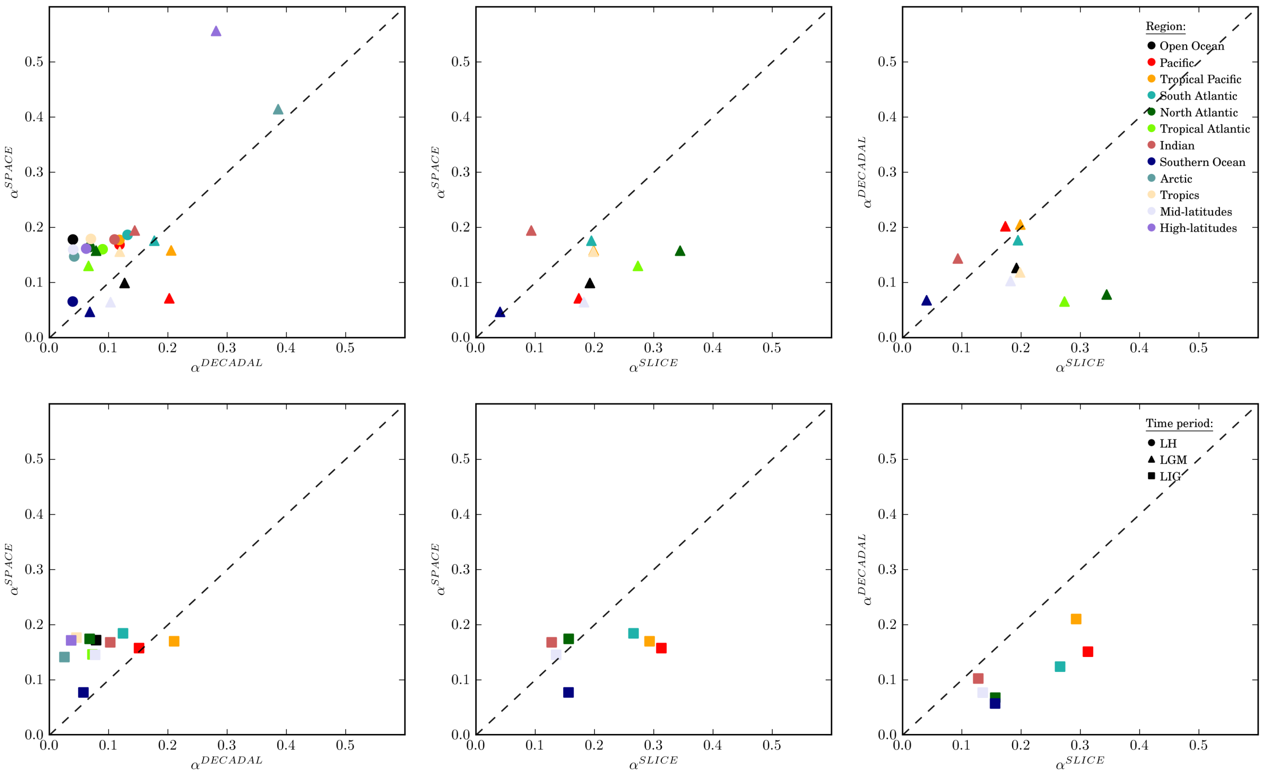

Arctic LGM-LH = -0.69
High LGM-LH = -0.19

Open LIG-LH = 2.05
Trop Atl LIG-LH = -0.25

Arc LIG-LH = 2.34
Trop LIG-LH = -0.39
High LIG-LH = -0.39

Figure 3: Comparison of spatial and temporal δ_{Ow}-salinity gradients; α^{SPACE} (the relative co-variability of δ_{Ow} and salinity over a region), $\alpha^{DECADAL}$ (the decadal co-variability of δ_{Ow} and salinity at a given point in space), and α^{SLICE} (the actual relationship between δ_{Ow} and salinity between the Last Glacial Maximum and Late Holocene [LGM-LH] or Last Interglacial and Late Holocene [LIG-LH] at a given point in space). Top panels show the LGM gradients as filled triangles (far left panel also shows LH gradients as filled circles). Bottom panels show the LIG gradients as filled squares. Left panels: difference between α^{SPACE} and $\alpha^{DECADAL}$ for each ocean region, representing the difference between the δ_{Ow} residual method, based on modern spatial gradients, and decadal δ_{Ow}-salinity co-variability. Middle panels: as left but between α^{SPACE} and α^{SLICE}, representing the comparison between the δ_{Ow} residual method and the actual modelled δ_{Ow}-salinity gradient. Right panels: as left and middle but between $\alpha^{DECADAL}$ and α^{SLICE}. Regional values of α^{SLICE} for the LGM-LH and LIG-LH that lie outside the axis limits on the middle and right panel are quoted below the figure. Filled colours denote each region that the gradient has been averaged over and are shown in the legend on the far right. The one-to-one line, representing perfect agreement between gradients, is also plotted (black dashed line).

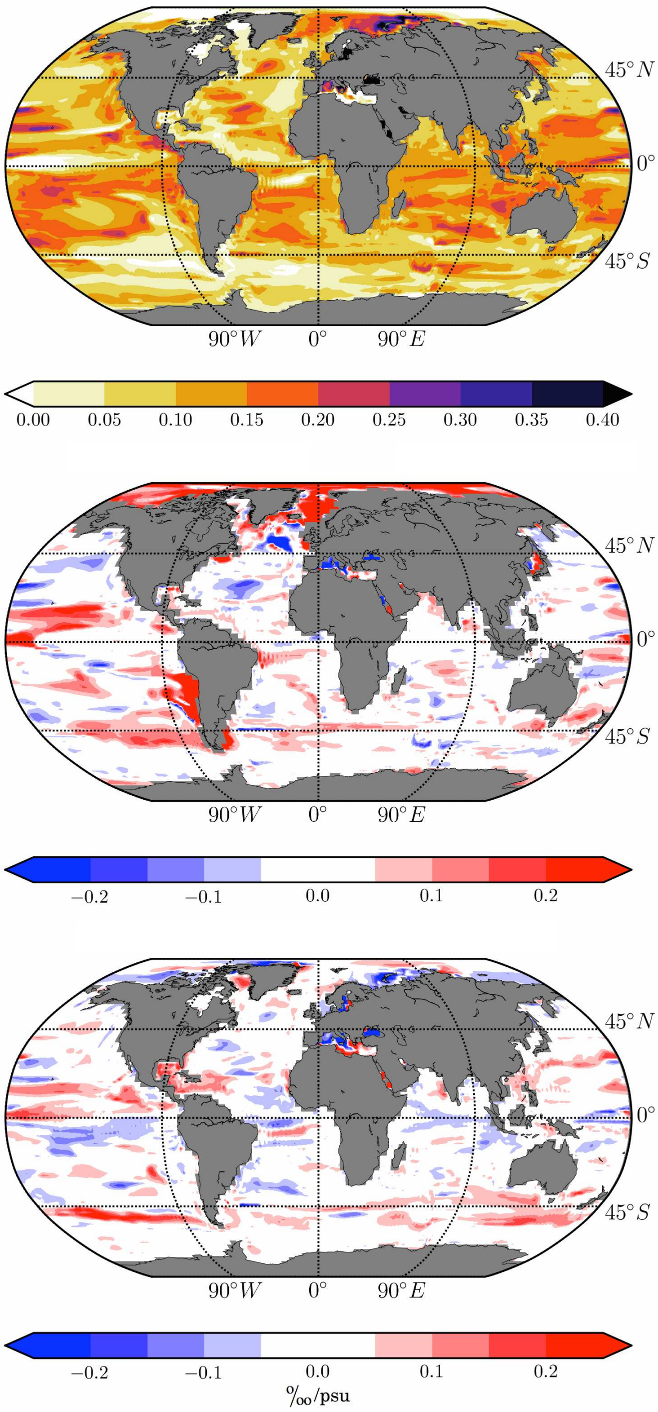

Figure 4: Multi-decadal co-variability of salinity and δ_{Ow} at each model grid point. Top: Gradient of the local linear regression on multi-decadal variability between sea surface salinity and sea surface δ_{Ow} over the last 100 years of the LH simulation ($\alpha_{LH}^{DECADAL}$). Middle: Difference in $\alpha^{DECADAL}$ between the LGM and LH simulations ($\alpha_{LGM-LH}^{DECADAL}$). Bottom: Difference in $\alpha^{DECADAL}$ between the LIG and LH simulations ($\alpha_{LIG-LH}^{DECADAL}$).

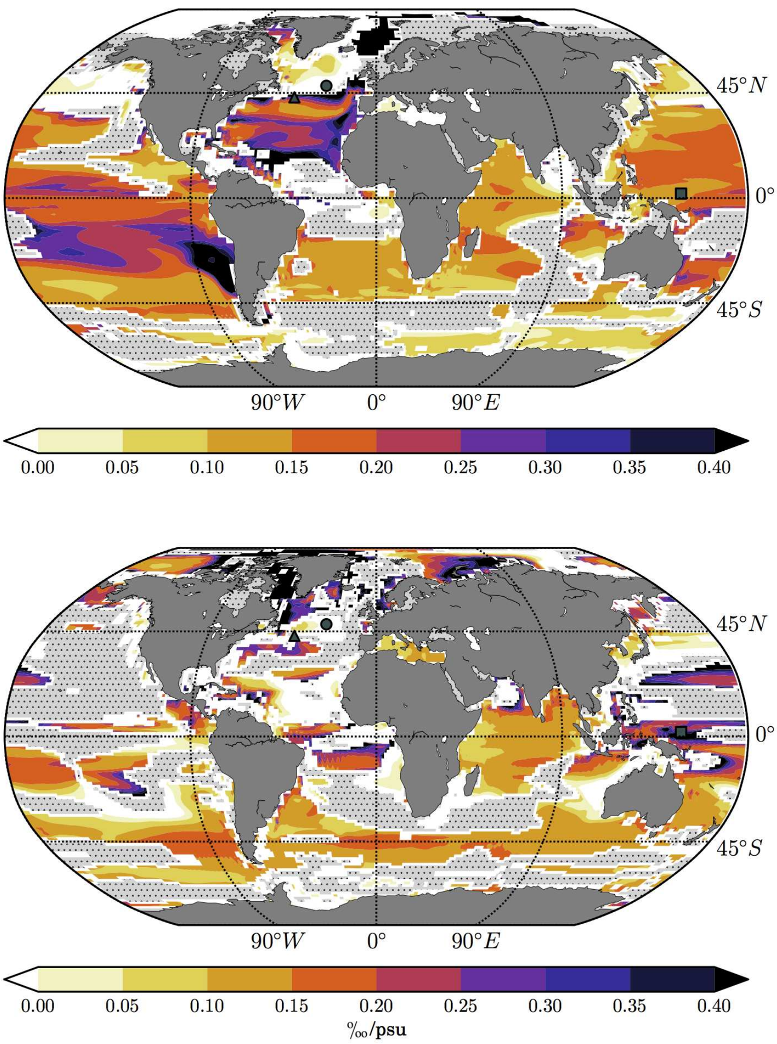

Figure 5: Modelled temporal δ_{Ow}-salinity gradient (α^{SLICE}) between the LGM and LH (top; α^{SLICE}_{LGM-LH}) and LIG and LH (bottom; α^{SLICE}_{LIG-LH}). Regions are masked where the change in salinity is small using a threshold of 0.1σ for the LGM-LH (0.24 psu) and 0.14σ for the LIG-LH (0.11 psu). A filled black circle, triangle, and square represent the locations plotted in the left, middle and right panels of Figure S3 respectively (see Supplementary Information).

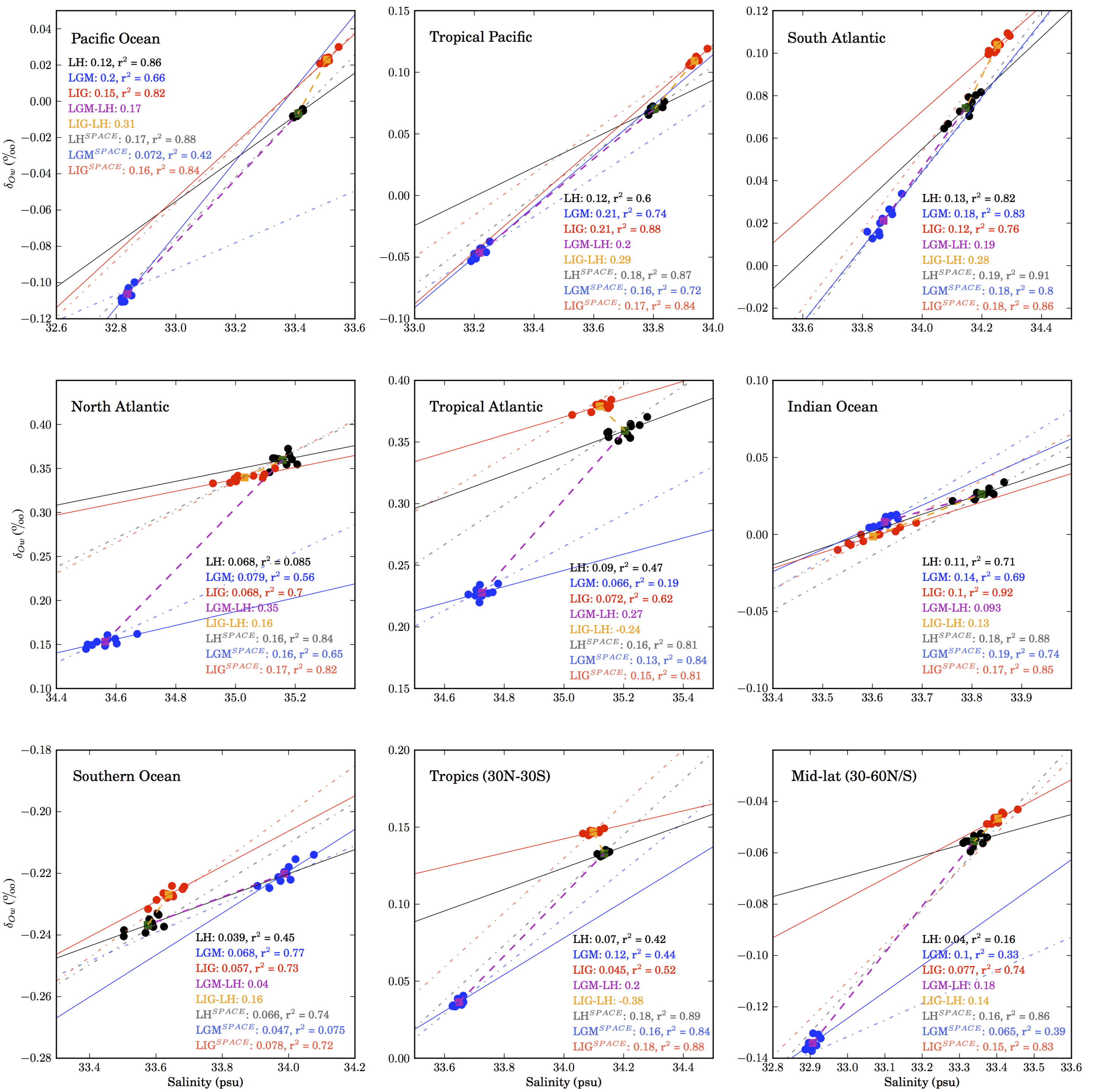

Figure 6: Variability between δ_{Ow}-salinity gradients across selected ocean regions. Filled circles represent decadally averaged δ_{Ow} and salinity values for the LH (black), LGM (blue) and LIG (red). Filled squares represent average δ_{Ow} and salinity values calculated over the final 100 years of the LH (green), LGM (mauve) and LIG (orange) simulations. Lines show the linear relationships between multi-decadal data (solid lines), centennially averaged data (dashed lines), and spatially averaged data (light grey, light blue and light red for LH, LGM, and LIG respectively, dot-dashed lines). The values of α^{SPACE}, $\alpha^{DECADAL}$, and α^{SLICE} are also shown on the figure with the associated r^2 values for $\alpha^{DECADAL}$ and α^{SPACE}.

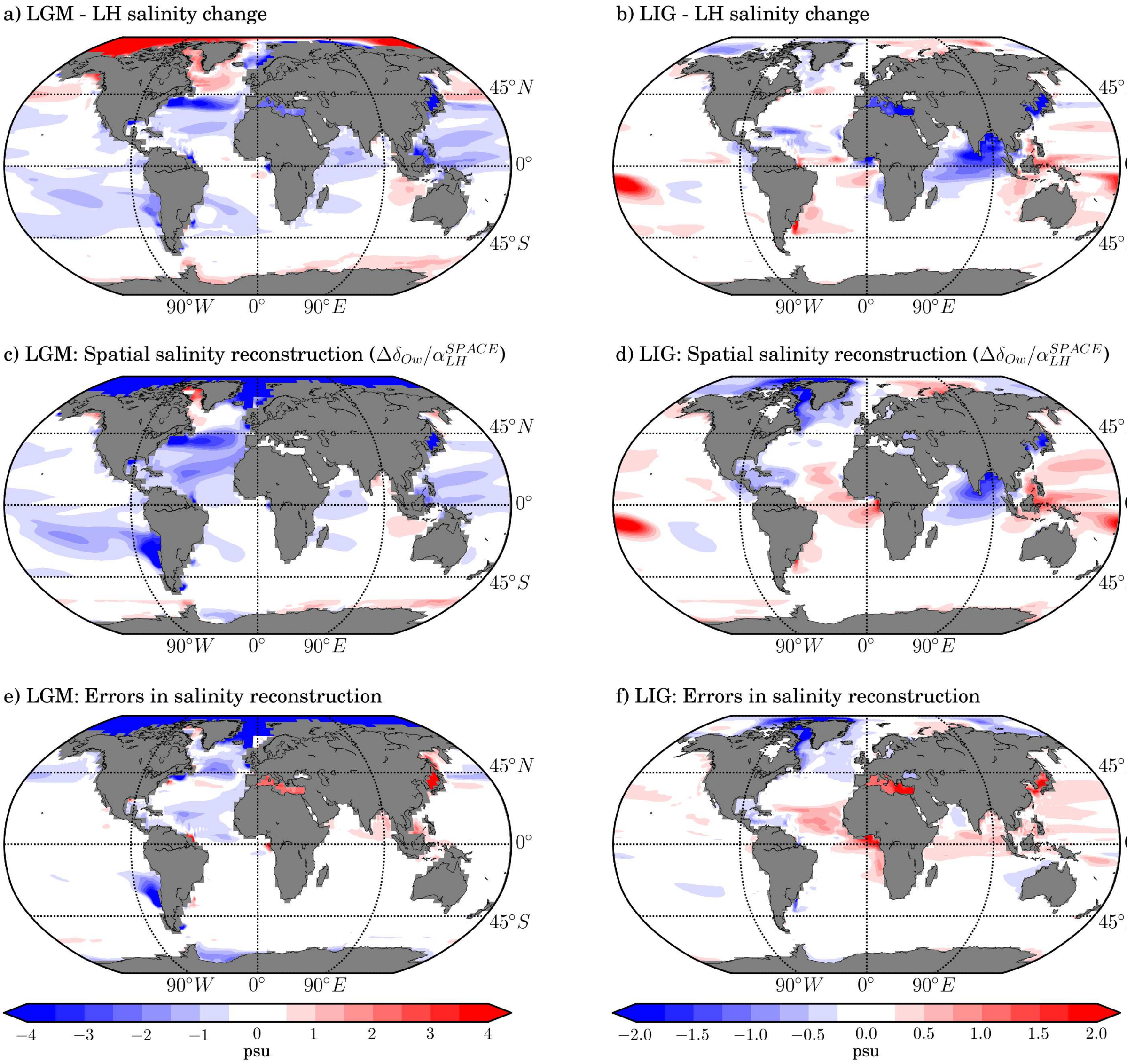

Figure 7: The δ_{Ow} residual method. Top panels: Salinity anomalies between a) the LGM-LH and b) the LIG-LH. Middle panels: Inferred salinity anomalies using the δ_{Ow} residual method for c) the LGM and d) the LIG (calculated by applying the LH spatial slopes to the LGM-LH and LIG-LH δ_{Ow} anomalies respectively). Bottom panels show the difference between the modelled salinity anomalies (top panels) and inferred salinity anomalies using the δ_{Ow} residual method (middle panels) for e) the LGM-LH and f) the LIG-LH. For subplots c-f, spatial slopes are calculated regionally over the North Atlantic, South Atlantic, Tropical Atlantic, extratropical Pacific, Tropical Pacific, Indian, Southern and Arctic Ocean (see Supplementary Information). Estimated salinity anomalies for areas of the surface ocean outside these regional definitions and in marginal seas were calculated using the open ocean spatial slope.